SPECIAL
Climate and Frontal Air-Sea Interaction
COLLECTION

Eddy–Wind Interaction in the California Current System: Dynamics and Impacts

HYODAE SEO

Woods Hole Oceanographic Institution, Woods Hole, Massachusetts

ARTHUR J. MILLER AND JOEL R. NORRIS

Scripps Institution of Oceanography, La Jolla, California

ABSTRACT

The summertime California Current System (CCS) is characterized by energetic mesoscale eddies, whose sea surface temperature (SST) and surface current can significantly modify the wind stress and Ekman pumping. Relative importance of the eddy–wind interactions via SST and surface current in the CCS is examined using a high-resolution (7 km) regional coupled model with a novel coupling approach to isolate the small-scale air–sea coupling by SST and surface current. Results show that when the eddy-induced surface current is allowed to modify the wind stress, the spatially averaged surface eddy kinetic energy (EKE) is reduced by 42%, and this is primarily due to enhanced surface eddy drag and reduced wind energy transfer. In contrast, the eddy-induced SST–wind coupling has no significant impact on the EKE. Furthermore, eddy-induced SST and surface current modify the Ekman pumping via their crosswind SST gradient and surface vorticity gradient, respectively. The resultant magnitudes of the Ekman pumping velocity are comparable, but the implied feedback effects on the eddy statistics are different. The surface current-induced Ekman pumping mainly attenuates the amplitude of cyclonic and anticyclonic eddies, acting to reduce the eddy activity, while the SST-induced Ekman pumping primarily affects the propagation. Time mean–rectified change in SST is determined by the altered offshore temperature advection by the mean and eddy currents, but the magnitude of the mean SST change is greater with the eddy-induced current effect. The demonstrated remarkably strong dynamical response in the CCS system to the eddy-induced current–wind coupling indicates that eddy-induced current should play an important role in the regional coupled ocean–atmosphere system.

1. Introduction

Oceanic mesoscale eddies, with a typical length scale of 10–100 km in the midlatitudes and 1000 km in the tropics, have signatures both in sea surface temperature (SST) and surface currents. The eddies interact with the atmosphere through the SST and surface current influencing wind stress, the process referred to in the literature as eddy–wind interaction or mesoscale air–sea interaction. This is conveniently represented in the form of bulk parameterization of the wind stress (ignoring the wave effects on currents) as

$$\tau = \rho_a C_D (W - U)|W - U|, \qquad (1)$$

where τ is the wind stress, ρ_a is the density of the air, C_D is the drag coefficient, and W and U are the 10-m wind speed and the surface current speed, respectively. The ocean eddies influence the wind stress through SSTs modifying W via marine boundary layer (MABL) dynamics (e.g., Wallace et al. 1989; Samelson et al. 2006) and surface currents creating velocity shear across the air–sea interface.

To illustrate the SST effect on the wind stress, suppose the total W and SST (T) are the sum of a background part b that is driven only by large-scale processes and an eddy part e that relates the W response to T_e, such that $T_{tot} = T_b + T_e$ and $W_{tot} = W_b + W_e$. The correspondence of W_e to T_e has been widely studied since Wallace et al. (1989) and Hayes et al. (1989), with the increase (decrease) in wind speed (stress) over the warmer (cold) side of the front and eddies via the change in turbulent heat flux, stability of the MABL, and downward

Corresponding author address: Hyodae Seo, 266 Woods Hole Road, MS 21, Woods Hole, MA 02543.
E-mail: hseo@whoi.edu

turbulent momentum transfer. The coherent wind response to mesoscale SST has been broadly observed in the global oceans (e.g., Park and Cornillon 2002; Xie 2004; Chelton and Xie 2010; O'Neill et al. 2010, 2012; Frenger et al. 2013; among many others).

Using this positive correlation between T_e and W_e, Chelton et al. (2004) developed an empirical relation that the spatial derivative of wind (vorticity or divergence) is linearly proportional to the SST gradient. This linear proportionality has been the standard metric to measure air–sea coupling on oceanic mesoscales (e.g., Maloney and Chelton 2006; Small et al. 2008; Song et al. 2009). In the California Current System (CCS), considerable SST anomalies and their gradients are found in the vicinity of the upwelling fronts, eddies, and filaments (e.g., Strub and James 2000; Castelao et al. 2006). In such regions, the wind stress curl and divergence fields are linearly proportional to the crosswind and downwind SST gradients, respectively (Chelton et al. 2007; Seo et al. 2007b; Haack et al. 2008; Boé et al. 2011). The SST-driven wind stress curl then leads to a perturbation Ekman pumping velocity (Chelton et al. 2001), which according to a recent survey of satellite observations by Gaube et al. (2015) produces a dipolar structure of Ekman pumping over an eddy. This perturbation Ekman pumping is known to influence the evolution and propagation of an eddy (Dewar and Flierl 1987). In the CCS, Chelton et al. (2007) estimated from satellite observations the summertime SST-induced Ekman pumping velocities to be $O(0.15)\,\mathrm{m\,day}^{-1}$. The perturbation Ekman pumping velocities have a greater range of variability than that driven by the large-scale wind stress, suggesting the important role by the eddy-induced SST–wind coupling in the upwelling and the CCS circulation system.

Jin et al. (2009) applied this observed empirical SST–wind stress relationship to an idealized upwelling problem for an eastern boundary current system. The result shows that the SST–wind stress interaction weakens the coastal upwelling largely because the upwelling-favorable nearshore wind stress is weakened in the nearshore zone because of the cold upwelled SSTs. The resulting increase in wind stress curl broadens and amplifies the poleward undercurrent as would be expected from the Sverdrup balance. Cyclonic eddies featuring relatively stronger SST gradients are found to be more strongly damped by the SST–wind stress coupling, resulting in a relative abundance of anticyclonic eddies in the equilibrium state. The overall impact of SST–wind interaction is to reduce eddy kinetic energy (EKE) by 25%. Note, however, that the SST fields used to modify the wind stress contain both the background condition (cold nearshore and warm offshore) as well as the eddies and fronts; hence, a question remains about the true effect of the "small-scale eddies."

Now suppose the ocean current U is the sum of the background U_b and the eddy-induced surface current U_e. Both components can affect the wind stress through (1). Pacanowski (1987) examined the large-scale effect of the relative motion in the wind stress formulation for the tropical Atlantic Ocean from an ocean general circulation model (OGCM). The inclusion of surface currents, again without distinction between background and eddies, reduces the effective wind stress imparted to the ocean and thus slows the surface currents by 30%. Luo et al. (2005) tested this effect in a coupled general circulation model (CGCM), showing that the prevailing easterly wind stress in the equatorial Pacific is reduced, resulting in slower currents and the reduced equatorial upwelling. This alleviates the cold bias in their model. Similar results have been obtained from numerous ocean modeling studies taking into account the surface current in the wind stress parameterization (e.g., Duhaut and Straub 2006; Hughes and Wilson 2008; Hutchinson et al. 2010; Zhai and Greatbatch 2007; Anderson et al. 2011). Kelly et al. (2001) and Cornillon and Park (2001) demonstrate from the scatterometer measurements of wind stress that the U_e of an eddy can be inferred from the wind stress based on the fact that the scatterometer estimates the wind velocity relative to the ocean surface velocity. An OGCM simulation by Eden and Dietze (2009) shows that the EKE is weakened by 10% in the North Atlantic and by as much as 50% in the tropics when the current–wind interaction is included. This reduction was ascribed to the enhanced surface drag by the ocean eddies, while the reduction in barotropic instability due to the reduced lateral shear of the mean currents was of secondary importance. Again, none of these studies attempted to separate the effect of U_b and U_e.

Eddy-induced SST T_e and surface current U_e both affect the Ekman pumping velocities but in different ways. Gaube et al. (2015) considered three mechanisms by which the ocean eddies affect the Ekman pumping, that is, 1) the eddy-induced SST, 2) the relative motion between wind and current, and 3) the gradient of relative vorticity (Stern 1965; McGillicuddy et al. 2007). The first process was already discussed in terms of the SST–wind coupling, while the last two arise from U_e. Gaube et al. (2015) show that these two U_e induced Ekman-pumping velocities are greater than that due to T_e for both the cyclonic and anticyclonic eddies. The current-driven Ekman pumping velocities are of the opposite sign to the surface vorticity of the eddy, resulting in divergence (convergence) of the surface current and consequent upwelling (downwelling) at the center of an anticyclone (cyclone). The net impact is to weaken the amplitude of the eddies (Martin and Richards 2001; McGillicuddy et al. 2007; Ledwell et al. 2008;

McGillicuddy 2015). Dewar and Flierl (1987) demonstrated that the momentum transfer to the oceans affected by T_e and U_e exerts distinctive feedback effects on the evolution and intensity of the eddy; the U_e leads to decay of the eddy via enhanced top-drag (Bye 1986), while the T_e, via change in drag coefficients and wind stress, affects the propagation of the eddy.

Some earlier studies suggest that T_e and U_e effects are not independent. For example, a regional coupled modeling study for the tropical Atlantic by Seo et al. (2007a) showed that the cold (warm) anomalies associated with the tropical instability waves (TIWs) are accompanied by an anomalous northward (southward) surface current concurrent with anomalous southward (northward) surface wind. The former is driven by the instability of the equatorial ocean leading to an anomalous eddy surface current, while the latter is driven by the wind response to the eddy-induced SST anomalies; therefore, the current–wind coupling is initiated by the SST–wind coupling. The resultant negative correlation between wind (stress) and the surface currents on the TIW spatiotemporal scales weakly damps the EKE. Small et al. (2009) found this understress effect that damps the wave energetics to be even stronger than the original estimate by Seo et al. (2007a) and to be comparable to the energy conversion process during baroclinic instability, the primary energy source of the waves.

These studies suggest consistent results; the inclusion of surface current or SST reduces the energetics of mesoscale eddies and currents via enhanced drags and the modified Ekman pumping. However, ocean-only simulations or coarse-resolution global coupled models used in the earlier studies do not properly capture the simultaneous and mutually dependent effects of the eddy-driven SST and surface currents on the wind speed, the stress, and their rectified effect on the energetics of the ocean. There has been no explicit attempt yet to separate the coupling effects on small-scale versus background scale. This study uses a high-resolution fully coupled ocean–atmosphere model with a novel scale-selective coupling strategy in an attempt to address these issues.

The paper is organized as follows: Section 2 describes the regional coupled model and the experimental configuration. Section 3 examines the mean state changes. Section 4 discusses the mechanism for change in EKE, and section 5 examines the Ekman pumping velocities. Section 6 is a summary and discussion of implications.

2. Model, experiments, and data

a. Model description

We utilize the Scripps Coupled Ocean–Atmosphere Regional (SCOAR) model (Seo et al. 2007b, 2014).

SCOAR currently couples one of two weather models, the Weather Research and Forecasting (WRF) Model (Skamarock et al. 2008) or the Regional Spectral Model (RSM; Juang and Kanamitsu 1994), to the Regional Ocean Modeling System (ROMS; Haidvogel et al. 2000; Shchepetkin and McWilliams 2005). This study uses the WRF–ROMS version of SCOAR (Seo et al. 2014). The interacting boundary layer between WRF and ROMS is based on bulk aerodynamic formulae (Fairall et al. 1996, 2003) that calculate surface fluxes of momentum, turbulent and radiative heat, and freshwater based on the near-surface meteorological variables provided by WRF. ROMS is driven by these surface fluxes and, in turn, feeds back to WRF via the SST and surface current. The SCOAR model has been used in a wide range of coupled dynamics studies in the Indian Ocean (Seo et al. 2008b, 2009, 2014), the Pacific Ocean (Seo et al. 2007b; Putrasahan et al. 2013a,b), and the Atlantic Ocean (Seo et al. 2006, 2007a, 2008a; Seo and Xie 2011, 2013).

The SCOAR domain covers the U.S. West Coast (31.1°–46.8°N, 134.5°–116°W; Fig. 1). The horizontal resolutions in WRF and ROMS are identical 7 km with matching grids and land–sea masks. The 7-km resolution in the ocean and atmosphere captures mesoscale processes in the ocean and atmosphere as well as the complex coastline and major headlands that are important for alongshore variation in the near-coast wind (e.g., Koračin et al. 2004; Renault et al. 2016). The use of identical resolution and matching grid not only helps to maximize the effect of air–sea coupling given the simulated finescale SSTs by the ocean model, but it also eliminates the known issue of regridding wind near the steep orography and complex coastlines (e.g., Capet et al. 2004). It also helps to lessen the computing burden associated with regridding. The model coupling is activated every 6 h in order to account for the diurnal cycle. ROMS (WRF) is run with a stretched vertical grid with a total of 30 (29) vertical levels. Approximately 10 layers are allotted in the upper 150-m depth (below 750-m height).

b. Experimental setup

The experiments are designed to separate the T_e effect on the wind (and thus the stress) from the U_e effect. The five SCOAR experiments differ only in how the wind stress is calculated in the bulk parameterization equation [(1)] with a different combination of background and eddy parts of T and U (Table 1). In CTL, the full T and U are included, while the effect of T_e is suppressed in the noT_e experiment, and no effect of U_e is included in noU_e. Two additional runs are carried out; noT_eU_e omits both eddy components of T and U, and the noU_{tot} ignores total (both background and eddy) surface current, and thus it does not consider the relative
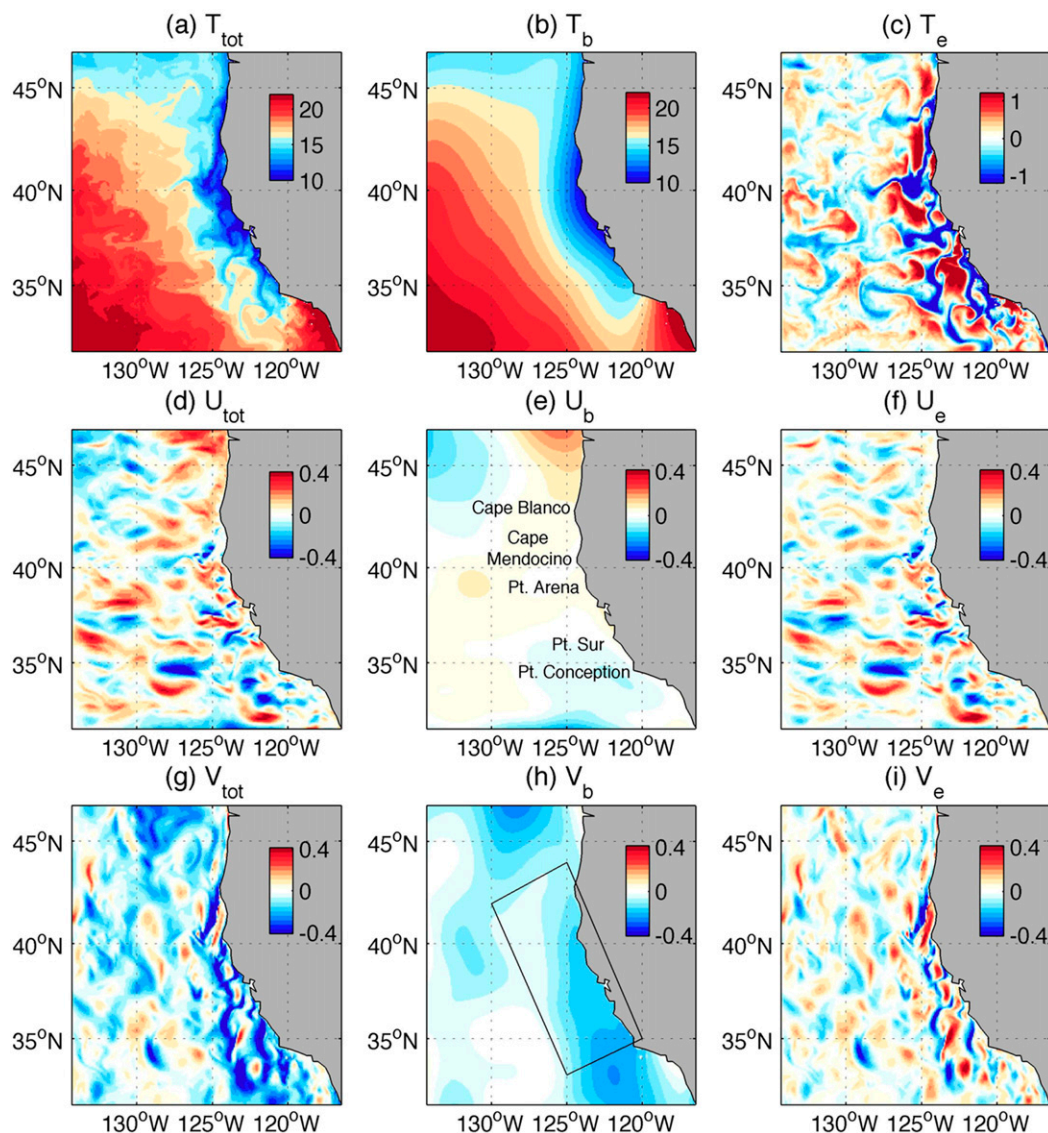
FIG. 1. Example of a 500-km lowess filtering applied to the daily snapshot (1 Aug 2008) of the ocean surface fields, (a)–(c) sea surface temperature T, (d)–(f) surface zonal current U, and (g)–(i) surface meridional current V. Left (center) column shows the fields before (after) the smoothing and the right column shows the difference (before minus after), that is, the small-scale fields of interest. The black box in (h) denotes the area to calculate the alongshore average of the EKE budget terms in Figs. 8 and 9.

motion of wind and current. The effect of T_e or U_e is then assessed from the statistical differences from the CTL; that is, CTL − noT$_e$ (CTL-noT$_e$) [CTL − noU$_e$ (CTL-noU$_e$)] reveals the net effect of T_e (U_e). Note that since ocean eddies occur spontaneously and randomly in each run, deterministic eddy-phase comparisons between runs are not useful.

c. 2D online smoothing

Separating the spatial scales of T and U during the coupled model integration requires an online spatial smoothing.

This is done by implementing an online smoothing technique in the SCOAR coupler. Figure 1 shows the examples of the fields before and after the smoothing. This technique was first used for SST fields in Putrasahan et al. (2013a,b); this study extends to surface currents. The online, 2D, spatial, locally weighted scatterplot smoothing (lowess) filter (Chelton and Schlax 1994; Schlax et al. 2001) with the tricubic weighting function of Cleveland (1979) and Cleveland and Devlin (1988) is applied only to the SST and surface currents produced by ROMS that are felt by the atmosphere at each coupling

TABLE 1. Description of the experiments performed in this study. The subscript b (e) denotes background (eddy) field. See section 2b for details.

Experiments	Surface temperature ($T = T_b + T_e$)		Surface current ($U = U_b + U_e$)	
		Wind stress formulation includes		
CTL	T_b	T_e	U_b	U_e
noT$_e$	T_b		U_b	U_e
noU$_e$	T_b	T_e	U_b	
noT$_e$U$_e$	T_b		U_b	
noU$_{tot}$	T_b	T_e		

step. Note that the actual SST and surface current in ROMS are left unchanged but evolve instead under the influence of the atmosphere that has seen only the smoothed SST and current fields. Therefore, it allows large-scale coupling effects to be preserved while suppressing the small-scale coupling via T_e and/or U_e. To the best of the authors' knowledge, this sort of modeling approach with both eddy SST and currents has not been attempted in any earlier studies. A loess filter with half-power filter cutoff wavelength of 500 km is used, yielding an effective cutoff wavelength of 300 km. Hence, in this study, processes on a length scale shorter than 300 km are regarded as small scale or eddies. The sensitivity of the result to different cutoff scales has also been assessed, for example, the 250-km lowess filter yielding the cutoff wavelength of 150 km. The results do not vary considerably with the chosen filtering scale as long as key finescale features are filtered.

It is important to note that our interest is to isolate the effect of eddies. In the sensitivity simulations, therefore, the coupling of the wind to the oceanic background SST and surface current is retained in association with the summertime upwelling condition and the CCS, respectively. This is different from Jin et al. (2009) on SST and most of the studies on surface current, where such a distinction is not explicitly made.

Note also that time-scale separation during the coupled integration is not possible. Therefore, the eddies in the online smoothing are defined as the deviation from the spatial mean. The eddies in the subsequent analyses are however treated as the deviation from the time mean. This mismatch between the definitions could affect the interpretation of our results. Nevertheless, the eddies in the CCS are known to have well-defined spatiotemporal scales (e.g., Kurian et al. 2011), so that eddies defined in either way are expected to be equivalent.

d. Experiment details

Prior to the coupled integration, ROMS is spun up for 20 yr with the climatological surface forcing of wind stress, heat, and freshwater flux derived from the

Comprehensive Ocean–Atmosphere Dataset (da Silva et al. 1994) and the climatological lateral boundary condition from the Simple Ocean Data Assimilation (SODA) monthly analysis version 2.2.4 (Carton and Giese 2008; Giese and Ray 2011). ROMS in the coupled run is initialized from the end state of the spinup simulation, representing the climatological condition of 1 January from the 20-yr spinup simulation. In the coupled configuration, ROMS is driven by the time-varying monthly $T/S/U/V$ from SODA and the interactive surface forcing from the WRF. The initial and boundary condition for WRF are from the 6-hourly National Centers for Environmental Prediction (NCEP) Operational Global Final Analyses dataset on a $1° \times 1°$ grid (http://rda.ucar.edu/datasets/ds083.2). Initialized from 1 January 2004, CTL is integrated for 7 yr until 31 December 2010. The last 6 yr of the simulations are analyzed, disregarding the first year as a coupled boundary layer spinup process. The sensitivity experiments branch off from the CTL beginning 1 January 2006 (i.e., after the 1 yr of the coupled spinup), from which the wind stress calculation is modified as described above for the following 6 yr.

WRF uses the new Kain–Fritsch cumulus scheme using a mass flux approach (Kain 2004) and the WRF single-moment 3-class scheme for cloud microphysics (Hong et al. 2004). The planetary boundary layer (PBL) is treated with the Yonsei University (YSU) nonlocal PBL scheme (Hong et al. 2006), run with the fifth-generation Pennsylvania State University (PSU)–National Center for Atmospheric Research (NCAR) Mesoscale Model (MM5) surface layer scheme based on Monin–Obukhov similarity theory (e.g., Beljaars 1995). The WRF Model is also run with the Rapid Radiation Transfer Model (RRTM; Mlawer et al. 1997) and the Goddard scheme (Chou and Suarez 1999) for longwave and shortwave radiation transfer through the atmosphere. The Noah land surface model is used for the land surface process (Chen and Dudhia 2001). The mixed layer dynamics of ROMS are parameterized using a K-profile parameterization (KPP) scheme (Large et al. 1994) including penetrative shortwave heating effects (Paulson and Simpson 1977). No explicit horizontal diffusivity is used, although the third-order upstream biased horizontal advection scheme introduces implicit numerical diffusivity (Haidvogel et al. 2000).

e. Datasets

Several observational products are used to validate the model basic states. To calculate the surface geostrophic current, we use the global sea surface height (SSH) anomaly dataset from Archiving, Validation, and Interpretation of Satellite Oceanographic Data (AVISO)

produced by Ssalto/Duacs with support from CNES (http://www.aviso.altimetry.fr). For this study, we use the SSH dataset from January 2005 to December 2010 with a weekly interval and a $\frac{1}{3}° \times \frac{1}{3}°$ spatial resolution. Surface wind and wind stress are obtained from the 3-day-averaged QuikSCAT satellite data on a $\frac{1}{4}° \times \frac{1}{4}°$ grid for January 2005 to November 2009, available from the Asia–Pacific Data-Research Center (APDRC) of the University of Hawaii. The NOAA Optimum Interpolation (OI) $\frac{1}{4}°$ daily SST (AVHRR only) is used for SST fields (Reynolds et al. 2007). The surface heat flux fields are obtained from the 1° OAFlux dataset (Yu and Weller 2007). All these observed datasets are linearly interpolated to the model grid.

3. Impact on climatologies

Figure 2 compares the model simulations with the observations for the summertime [July–September (JAS)] climatologies of SST, surface current, latent heat (LH) flux averaged for 2005–10, and wind stress averaged for 2005–09. The observed SST (Fig. 2a, shading) and surface currents (green vectors showing current speed exceeding $10 \, \mathrm{cm \, s^{-1}}$) are taken from the NOAA OI SST and the SODA ocean dataset. Comparison with other datasets for SST and surface currents [e.g., the SODA SST or the Ocean Surface Current Analyses–Real Time (OSCAR) current] reveals similar results (not shown). The observed SSTs and currents are overlaid with the QuikSCAT wind stress (brown vectors showing wind stress magnitude exceeding $0.075 \, \mathrm{N \, m^{-2}}$) and the latent heat flux from OAFlux (blue contours, negative ocean cooling).

The JAS SST fields represent the fully developed summertime upwelling condition, with lower SST along the U.S. West Coast north of Pt. Conception and warmer SSTs offshore. Regions of the nearshore SST minima are found in the lee of major coastal headlands such as Cape Blanco, Cape Mendocino, and Pt. Arena between 37° and 43°N, where the northerly/northwesterly wind stress is high (Koračin et al. 2004). The surface current is southwestward due to the wind-driven Ekman currents in response to the northerly/northwesterly wind. Currents at the deeper depth (e.g., 50 m) reveal the south/southeastward geostrophic California Current (not shown). The zonal extent and the alongshore variation of the nearshore cold SST correspond roughly to that of the offshore current. Latent heat flux reflects the SST pattern, cooling the ocean everywhere in the domain with minimum cooling ($<-25 \, \mathrm{W \, m^{-2}}$) in the nearshore upwelling zone and maximum cooling in the southwestern portion of the domain ($<-70 \, \mathrm{W \, m^{-2}}$).

CTL reproduces reasonably well the salient features of the summertime climatology in the CCS, although the

simulated SST is somewhat too cold in the nearshore upwelling zone and too warm far offshore toward the southwestern portion of the domain, leading to excessive latent cooling there. This strong east–west gradient is accompanied by more vigorous meanders of the CCS in the model than the observations. The simulated wind stress is also stronger than the QuikSCAT and is partly responsible for the stronger upwelling response.

Differences of the surface climatologies between CTL and two sensitivity runs (noT_e and noU_e) are shown in Figs. 2c and 2d. Recall that the CTL-noT_e (CTL-noU_e) represents the effect of T_e (U_e). Two coupling effects produce different time-mean (rectified) SST response patterns, although in both cases the SST difference fields are characterized as alternating bands of positive and negative values between the coast and 300–500 km offshore. The cold and warm SST anomalies coincide well with the southwestward and northeastward surface current anomalies (green vectors). Latent heat flux and wind stress (magnitude and direction) are in general a response to the change in SST, such that warm (cold) SST is collocated with the anomalous latent cooling (heating) and the southward (northward) wind stress anomalies, the latter being consistent with the MABL response to SSTs. The magnitude of the mean (rectified) SST change is greater from the U_e effect than the T_e effect, suggesting that U_e causes a stronger dynamical adjustment process in the CCS.

The physical processes that lead to different SST climatologies are examined from the mixed layer (ML) heat budget analysis. The vertically averaged ML heat budget equation is derived from the conservation of mass and heat equations (e.g., Moisan and Niiler 1998; Caniaux and Planton 1998) and is expressed as

$$
\begin{aligned}
\langle T \rangle_t = & -\langle \mathbf{u} \rangle \cdot \nabla \langle T \rangle - \frac{1}{h} \nabla \cdot \int_{-h}^{0} \tilde{\mathbf{u}} \tilde{T} \, dz \\
& - \frac{1}{h} [\langle T \rangle - T(-h)] w_e(-h) + \frac{1}{h} \overline{w'T'}(-h) \\
& + \frac{Q_0}{\rho_0 C_p h} + A_H \nabla^2 \langle T \rangle,
\end{aligned}
\tag{2}
$$

where the subscripts t and z denote partial derivatives in time and depth; $\mathbf{u} = (u, v)$ are the horizontal velocity components, w is the vertical velocity, ∇ is the horizontal gradient operator, ρ_0 is the density of seawater, C_p is its heat capacity, and A_H is the horizontal eddy diffusivity. The brackets $\langle \ \rangle$ denote the vertical average over the mixed layer depth (MLD), while tildes represent the deviation from the depth average. The MLD, $h(x, y, t)$, is estimated as the depth at which the density increases by $0.125 \, \mathrm{kg \, m^{-3}}$ from the surface value. The entrainment velocity at the ML base, $w_e(-h)$, is defined following Stevenson and Niiler
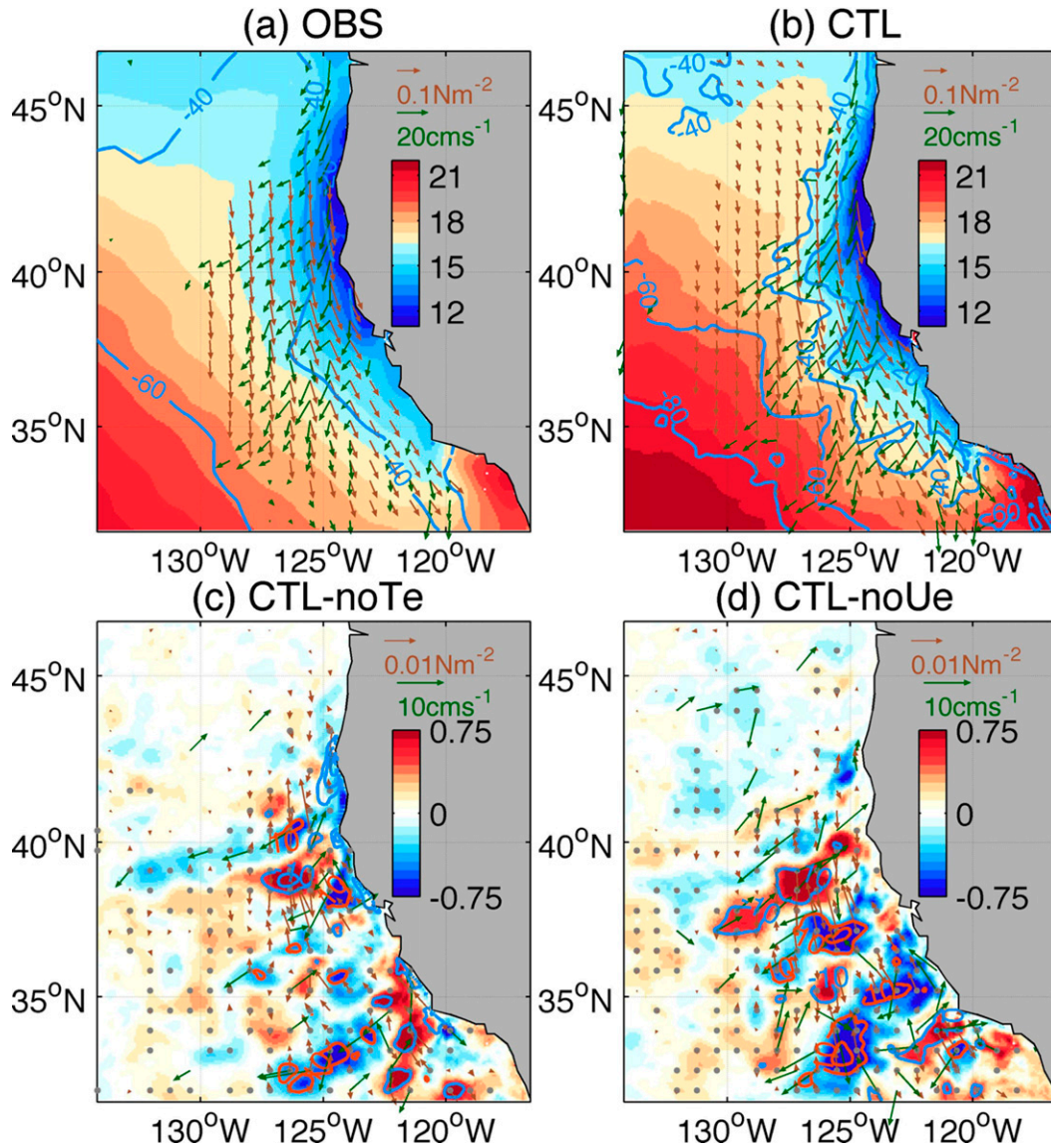
FIG. 2. (a) Observed summertime (July–September) SST (shading, °C, from NOAA OI SST), surface current (green vectors, cm s^{-1}, shown only when greater than 10 cm^{-1}, from SODA), latent heat flux (blue contours, W m^{-2}, contour interval (CI) = 20, negative cooling the ocean, from OAFlux), and wind stress vectors (brown vectors, N m^{-2}, shown only when greater than 0.075 N m^{-2}, from QuikSCAT). (b) As in (a), but from CTL. SST, current, and LH are for 2005–10, while wind stress is for 2005–09 to match the QuikSCAT period. Difference fields: (c) CTL − noT$_e$ and (d) CTL − noU$_e$. Gray dots denote the area of significant change in SST ($p = 0.05$) based on a two-sided Student's t test.

(1983) as $w_e(-h) = w(-h) + h_t + \mathbf{u}(-h) \cdot \nabla h - A_H \nabla^2 h$. The term Q_0 is the net surface heat flux corrected for the penetrative shortwave radiation though the ML base.

The ML temperature tendency on the left-hand side of (2) is determined by the terms on the right-hand side. The first two terms are the horizontal advections by depth-averaged current and by the deviation from the mean current. The third and fourth terms are the entrainment and the turbulent heat flux at the ML bottom.

The fifth and sixth terms are the heat flux absorbed in the ML and the horizontal heat diffusion.

No explicit horizontal diffusivity is used in the ROMS model; hence, $A_H = 0$. In the present analysis, the mean and eddy are defined as the time mean plus seasonal cycle (overbars) and the deviations from the seasonal cycle (primes), respectively, as opposed to the depth average and the deviation, as expressed in (2). Therefore, the total horizontal advection (the
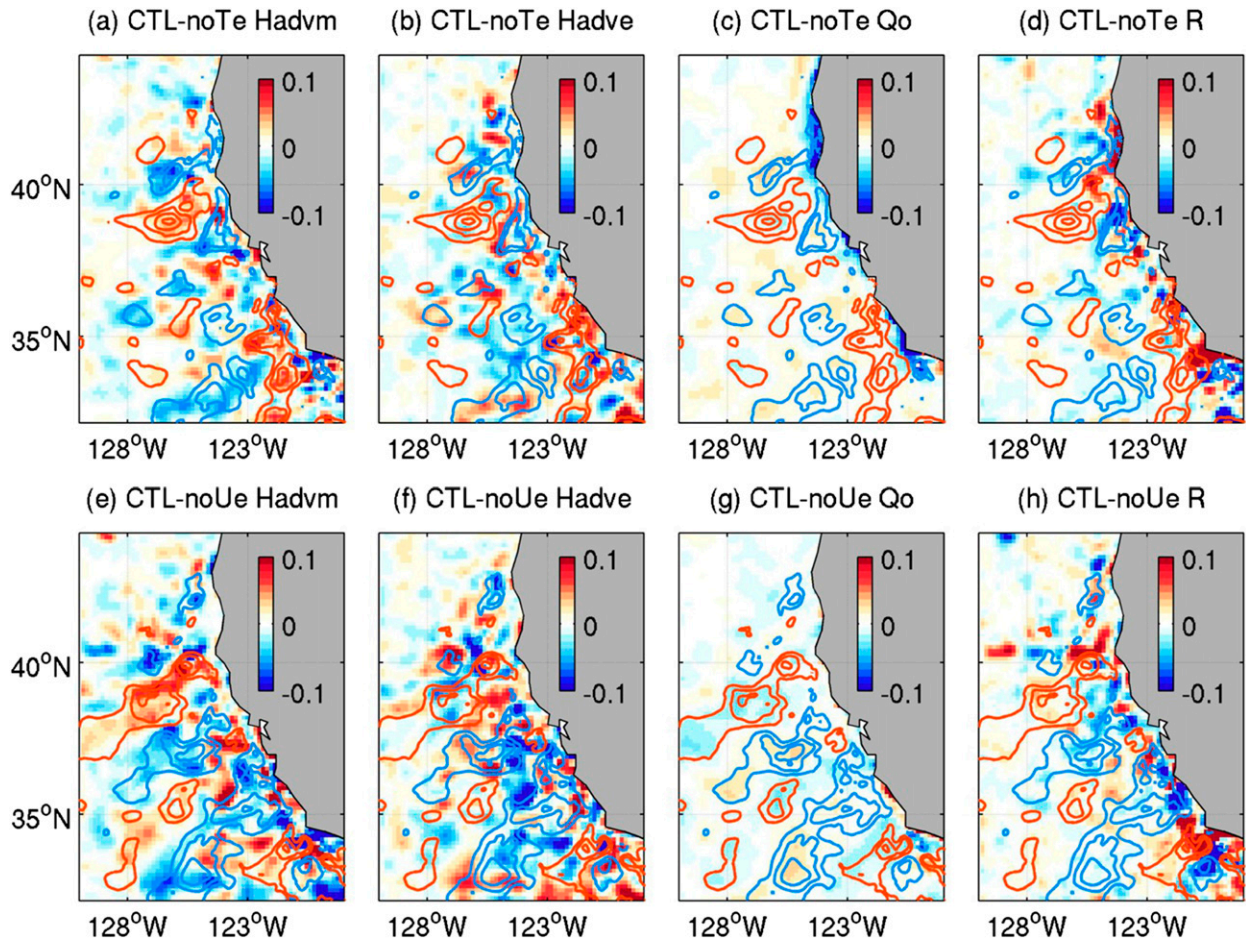
FIG. 3. Results from the summertime (July–September) mixed layer heat budget analysis showing the difference in the budget terms ($°C\,day^{-1}$): (top) CTL-noT$_e$ and (bottom) CTL-noU$_e$. (a),(e) Mean horizontal advection (Hadvm); (b),(f) eddy horizontal advection (Hadve); (c),(g) net heat flux (Q_0); and (d),(h) the residual (R). The red (blue) contours denote the corresponding positive (negative) changes in SST (CI = 0.3°C beginning from ±0.3°C).

sum of the second and the third terms) is written as $-(1/h)\int_{-h}^{0}(\overline{u\cdot\nabla T} + u'\cdot\nabla\overline{T} + \overline{u}\cdot\nabla T' + \overline{u'\cdot\nabla T'})\,dz$. Since the ML heat budget is calculated based on the 3-daily and spatially subsampled fields, it is difficult to reliably estimate the terms in $w_e(-h)$ and $(1/h)\overline{w'T'}(-h)$. To retain and focus on the terms that can be reliably estimated by the present analysis, the vertical processes leading to the heat flux out of the ML base are estimated as the residual R. The lack of estimate for vertical process is a caveat of the analysis provided here. In addition to entrainment and turbulent heat flux, R would also include contributions from numerical errors associated with the discretization and interpolation as well as the implicit horizontal diffusion inherent to the advection scheme of the ROMS model (Haidvogel et al. 2000). In the nearshore upwelling region, it is reasonable to assume that R is dominated by entrainment; R is strongest in the nearshore region and

negligible offshore (not shown). The simplified version of the heat conservation equation is expressed as

$$\langle T\rangle_t = -\frac{1}{h}\int_{-h}^{0}(\overline{u\cdot\nabla T} + u'\cdot\nabla\overline{T} + \overline{u}\cdot\nabla T' + \overline{u'\cdot\nabla T'})\,dz$$
$$+ \frac{Q_0}{\rho_0 C_p h} + R. \tag{3}$$

Figure 3 shows the differences in JAS horizontal advection by mean currents and eddies, surface heat flux, and the residual. Change in $\langle T\rangle_t$ is small compared to these terms and is not shown. Each plot is overlaid with the time-mean difference in SST. In both cases, the alternating bands of cold and warm SST anomalies (Fig. 2) tend to be collocated with the changes in mean horizontal advection having the same sign with the SST change. Pattern correlation suggests that the change in mean
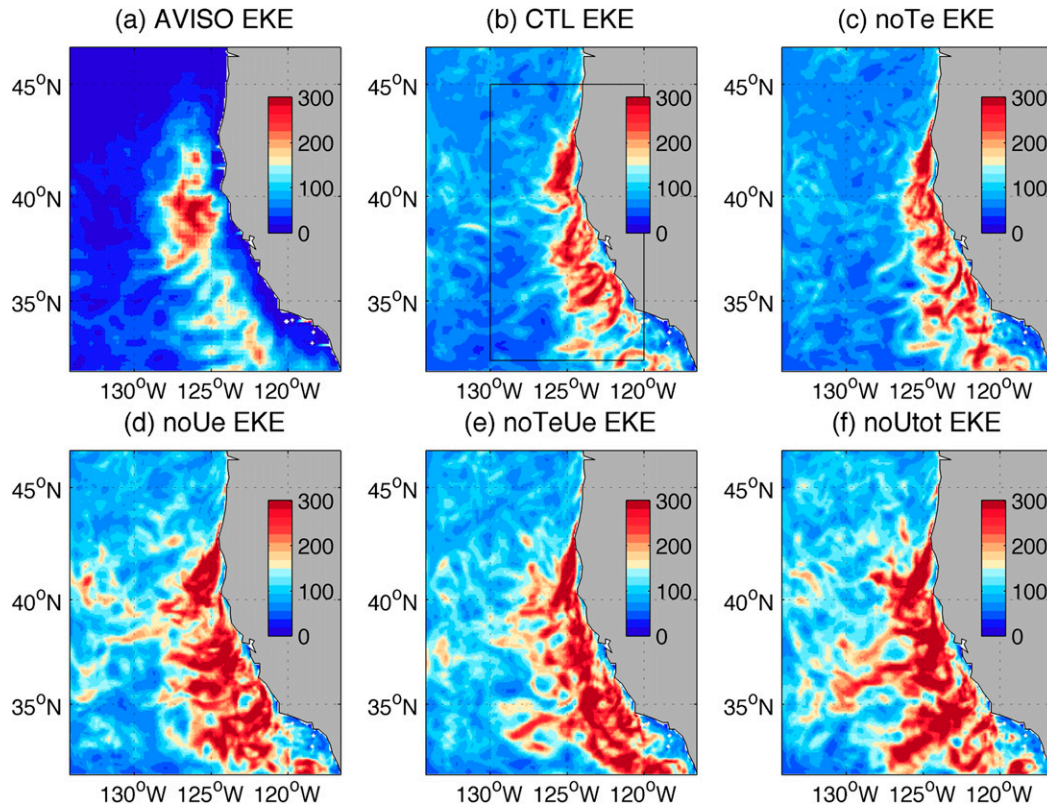
FIG. 4. (a) The summertime (July–September, 2005–10) surface EKE (cm^2 s^{-2}) derived from the altimeter dataset assuming geostrophy. (b)–(f) Simulated surface EKEs. The black box in (b) denotes the area to calculate the mean EKE in Table 2 and Fig. 6 (32°–45°N and 130°–120°W).

horizontal advection is significantly ($p = 0.01$) correlated with the change in SST (0.30 for CTL-noT$_e$ and 0.18 for CTL-noU$_e$). Eddy currents tend to have the opposite sign as the mean current but with the comparable magnitudes. The surface heat flux weakly offsets the effect of the mean currents and damps the SST anomalies. Change in the vertical processes in R is strong but limited to the shelf region. The CTL-U$_e$ case, in general, shows greater changes in horizontal mean and eddy currents compared to CTL-T$_e$; U_e produces a stronger dynamical ocean response through coupling with the wind stress. This is examined further in the following section.

Overall, the SST–wind and current–wind coupling effects generate different time mean–rectified SST response patterns, which are determined by the differences in advection of the altered wind-driven mean currents and the associated eddies. Since air–sea interaction arises from the altered SST fields brought about by the changes in mean and eddy advection, the following sections investigate the change in eddy energetics and the resultant ocean–atmosphere coupling.

4. Eddy variability

a. Impact on eddy kinetic energy

Figure 4 compares the JAS surface EKE per unit mass: EKE $= (1/2)(\overline{u'} + \overline{v'})$. From the AVISO sea level anomaly, surface EKE is derived assuming geostrophy (i.e., Ekman current variations are not included in this estimate). In CTL, high EKE is found all along the U.S. West Coast, with an area-averaged (32°–45°N and 130°–120°W; the box in Fig. 4b) surface EKE of 225 cm^2 s^{-2}. This is generally in agreement with the altimeter-derived EKE despite the difference in sampling rate, resolution, and the data processing procedure. It is also comparable to the EKE estimates from drifter observations for the CCS (e.g., Marchesiello et al. 2003; Centurioni et al. 2008). Comparison between CTL and noT$_e$ shows that the EKE and its spatial distribution are very similar; that is, the T_e effect on the wind stress has a minimal influence on the simulated EKE. In contrast, noU$_e$ has a considerably higher EKE than CTL by about 42% (Table 2). This implies that including the effect of the eddy surface current in the wind stress results in a large weakening of the EKE. Since the effect by U_e is

TABLE 2. July–September (JAS) surface EKE averaged over 32°–45°N and 130°–120°W (the black box Fig. 1g). Percent change from CTL is shown in the parentheses.

Experiments	Surface EKE
CTL	117
noT_e	116 (−1%)
noU_e	166 (+42%)
noT_eUe	161 (+38%)
noU_{tot}	179 (+53%)

much stronger, noT_eU_e shows a similar level of EKE compared to noU_e, confirming that T_e has a small effect. The noU_{tot} run exhibits 53% stronger EKE than the CTL, indicating that most of the EKE reduction is done by eddies U_e rather than by the background current U_b.

Figure 5 compares the depth versus cross-shore section of the JAS EKE averaged in the alongshore direction between 30° and 45°N (Fig. 4b). The EKE is surface intensified and exhibits a maximum 50–100 km offshore. The noT_e case has essentially the same structure of EKE, while noU_e shows a much-enhanced EKE in the upper 50 m and extends deeper (cf. the isopleths of $100\,cm^2s^{-2}$) and farther offshore. The noT_eU_e case has nearly the same EKE distribution as noU_e, and noU_{tot} has slightly stronger EKE due to the additional effect of U_b.

Figure 6 shows a year-round time series of the monthly mean surface EKE averaged over 32°–45°N and 130°–120°W (Fig. 4b). The EKE levels have a strong seasonal cycle with the maxima in summer and the minima in winter. The EKE in CTL (red) and noT_e (orange) are again similar in both seasons, while the runs without ocean current effects (blue to green curves), whether background or eddy, all display the higher EKE. It is interesting to note that the EKE difference due to the surface current effect is even stronger in winter, while that due to the SST effect remains unimportant. This implies that in winter, while the SST–wind coupling effect ceases to be important because of the lack of upwelling and SST gradients, the current–wind coupling effect continues to affect the energetics of the CCS. A closer examination of the seasonality of the coupling effects is currently underway and will be reported elsewhere; this study focuses solely on the summertime upwelling season.

b. Role of wind forcing and instability on the EKE response

What causes the reduction of the summertime EKE with the inclusion of U_e but not of T_e? To understand the EKE damping mechanism by U_e, three key energy conversion terms are derived from the equations of
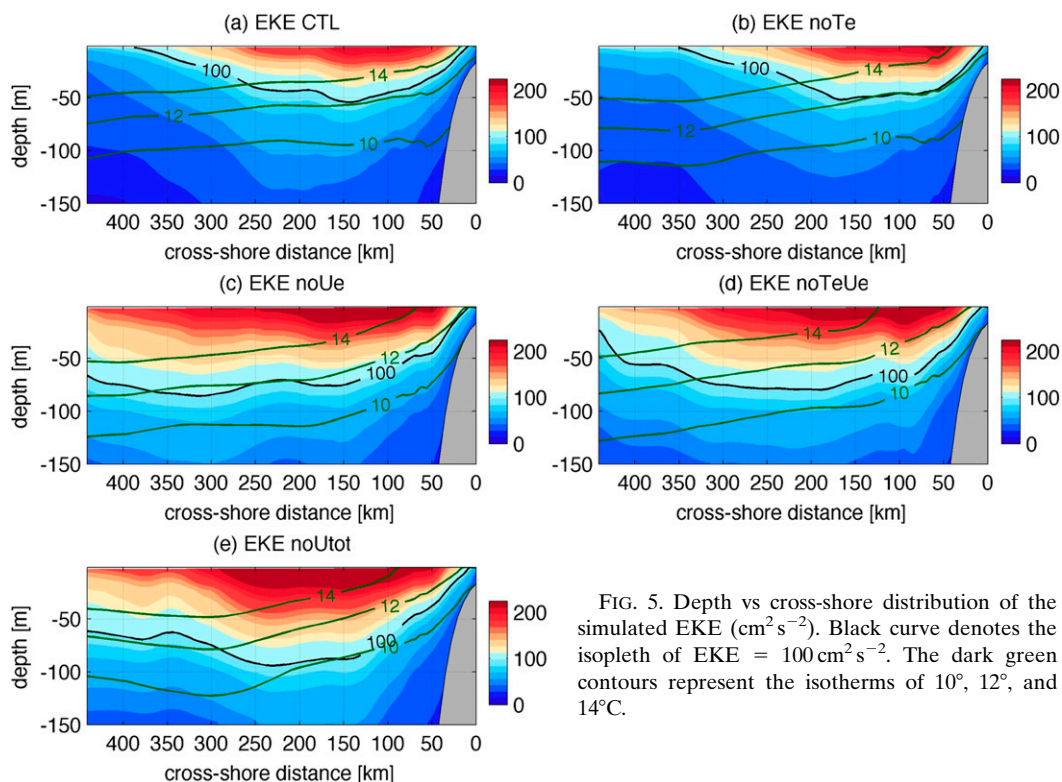

FIG. 5. Depth vs cross-shore distribution of the simulated EKE ($cm^2\,s^{-2}$). Black curve denotes the isopleth of EKE = $100\,cm^2\,s^{-2}$. The dark green contours represent the isotherms of 10°, 12°, and 14°C.

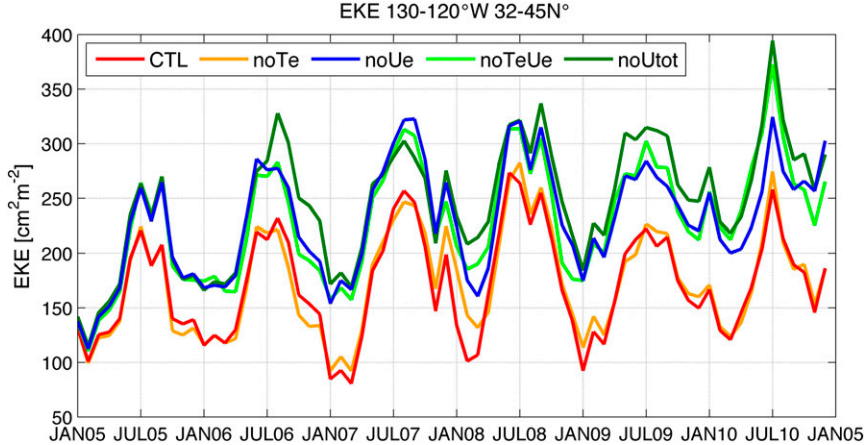FIG. 6. Monthly time series of the simulated surface EKE ($cm^2 s^{-2}$) averaged over the up-welling zone (32°–45°N, 130°–120°W; Fig. 4b).

motion following Masina et al. (1999) for the TIWs and Marchesiello et al. (2003) for the CCS eddies and are evaluated with the result from the model:

$$BC = -\frac{g}{\rho_0} \overline{\rho' w'}, \tag{4}$$

$$BT = -(\overline{u'u'U}_x + \overline{u'v'U}_y \overline{+ u'w'U}_z + \overline{v'u'V}_x$$
$$+ \overline{v'v'V}_y + \overline{v'w'V}_z), \quad \text{and} \tag{5}$$

$$P = \frac{1}{\rho_0} (\overline{u'\tau'_x} + \overline{v'\tau'_y}). \tag{6}$$

Here, the capital letters (U, V) denote the summer-time (JAS) climatology, and the primes are the deviation from the mean. The BC term represents an energy conversion process during baroclinic instability, whereby mean available potential energy is converted into EKE. The BT term represents the conversion of the mean kinetic energy to EKE, which is typically dominated by two processes: the horizontal and vertical Reynolds stresses indicative of (equivalent) barotropic instability and Kelvin–Helmholtz instability. The P term is the work done by the wind on the ocean, representing eddy–wind interactions. If positive, it supplies wind energy to the ocean and increases the EKE, thus serving as the wind work; if negative, it is part of the dissipation of the EKE. Assuming the length scale of the eddies to be the internal Rossby radius of deformation L, the depth H to which the terms (4)–(6) are to be averaged is determined by $H = fL/N$; using $f = 10^{-4}$, $L = 10^4$, and $N = 10^{-2}$, a characteristic depth scale of $H = 100$ m is obtained. Averaging over different depth ranges does not change the results considerably due to the similarity of the vertical structure in the EKE (Fig. 5).

Figure 7 shows the three energy conversion terms from CTL. Strongest near the coast north of San Francisco, P is the dominant source term for EKE. BC is of secondary importance over the shelf. The sum of the effects of barotropic and Kelvin–Helmholtz instabilities (BT) is small, perhaps because the model does not fully resolve the small-scale shear of the currents (Brink 2016; Brink and Seo 2016). Decomposition of P into the zonal $[P_x = (1/\rho_0)\overline{u'\tau'_x}]$ and the meridional $[P_y = (1/\rho_0)\overline{v'\tau'_y}]$ components suggests that, not surprisingly, most of the EKE increase is via the positive correlation between v' and τ'_y; that is, the alongshore current anomalies are generated as a response to the alongshore wind stress anomalies.

The zonal component P_x is weak but negative in the upwelling zone, which acts to dissipate the EKE. The negative correlation between u' and τ'_x is explained by the fact that the zonal current at the surface u' is in part a wind-driven Ekman response to southward τ'_y (Fig. 2); that is, when τ'_y is negative (upwelling favorable), the portion of u' that is driven by the Ekman transport is directed offshore. During typical upwelling conditions, τ'_x is weakly eastward since the large-scale wind stress is southeastward (Fig. 2). Thus, u' and τ'_x should be in the opposite direction during the upwelling conditions. This is evidenced by the fact that negative P_x is strong over the upwelling zone south of Cape Blanco, where the eastward component of the wind stress emerges in the lee of capes and with the southeastward bend of the coastline (Dorman and Koračin 2008). This implies that the inclusion of the surface current effect reflects not only the small-scale eddies (internal variability), but also the linear wind-driven Ekman component that is characteristic of summertime eastern boundary current systems. Therefore, some of the U_e effects discussed in this
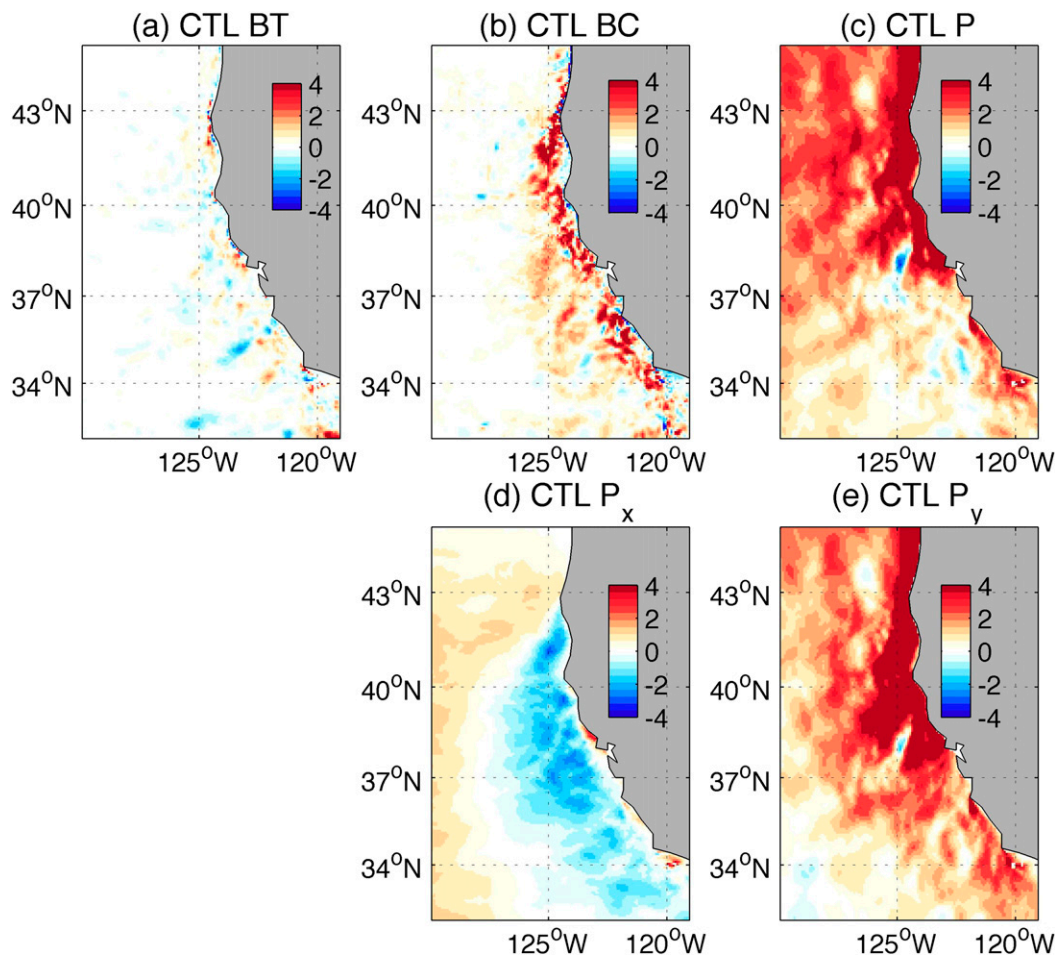
FIG. 7. Energy conversion terms ($10^{-8}\,\mathrm{m^2\,s^{-3}}$) calculated for the summer (July–September) 2005–10 from CTL. (a) BT denotes the sum of two energy conversions: barotropic and Kelvin–Helmholtz instabilities. (b) BC is the baroclinic instability; (c) the P term. (d)–(e) The zonal $[P_x = (1/\rho_0)\overline{u'\tau_x'}]$ and meridional $[P_y = (1/\rho_0)\overline{v'\tau_y'}]$ components of the P.

study might be predictable from the large-scale wind fields, given that the summer wind field is remarkably steady in the CCS (Chelton et al. 2007). However, the wind energy input is dominated by P_y.

Since P and BC are the two dominant sources of EKE, the following analysis will focus on these two terms. The subsequent analysis will also focus on CTL, noT$_e$, and noU$_e$ only, showing the starkest contrasts. Figure 8 shows EKE, BC, and P as a function of the offshore distance averaged along the coast between 35° and 45°N and over the upper 100-m depth. EKE peaks at 150 km offshore in all three runs, and noU$_e$ remains higher much farther offshore with a secondary peak at 300 km. Again EKE in CTL and noT$_e$ are nearly the same, and the noU$_e$ EKE is greater by about 56% when averaged over the offshore distance. BC peaks at about 50 km offshore in all three runs, coinciding with the location of the summertime upwelling front (Fig. 2). The BC then

rapidly decreases offshore out to 450 km. CTL and noT$_e$ show similar cross-shore profiles of BC with nearly the same cross-shore average values. On the other hand, noU$_e$ has lower BC with the largest reduction in the range between 100 and 200 km. The weaker BC in noU$_e$ is, therefore, unlikely to cause the higher EKE. In order for the BC to change significantly, there should be a strong change in alongshore wind stress via the SST–wind coupling relationship. This may occur when the effect of "broader-scale" cold SST in the upwelling zone is removed, as was done in Jin et al. (2009), but not on the oceanic eddy scales. The alongshore wind stress is not so much changed after all (Fig. 2).

Changes in eddy–wind interaction clearly explains the difference in the EKE. The P term is strongest near the shore at ~25 km. The P term in noT$_e$ is only slightly changed, suggesting that suppressing the T_e effect on the wind speed does not affect the wind–energy transfer,
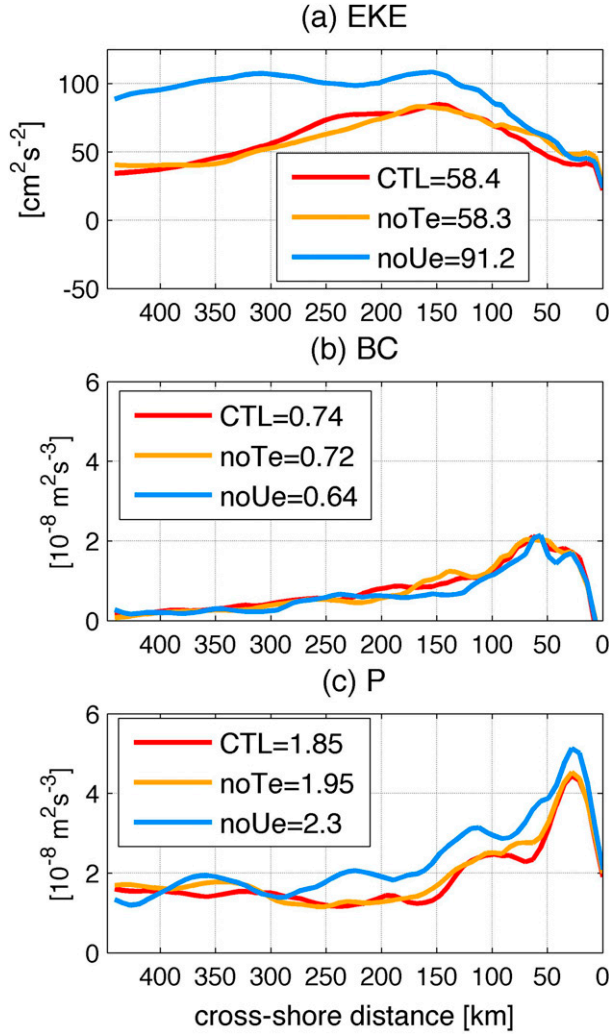
FIG. 8. Cross-shore distribution of the upper 100-m-averaged (a) EKE ($cm^2 s^{-2}$), (b) BC ($10^{-8} m^2 s^{-3}$), and (c) P ($10^{-8} m^2 s^{-3}$) during the summer (July–September) of 2005–10. The cross-shore averaged quantities are shown in the legend of each panel.
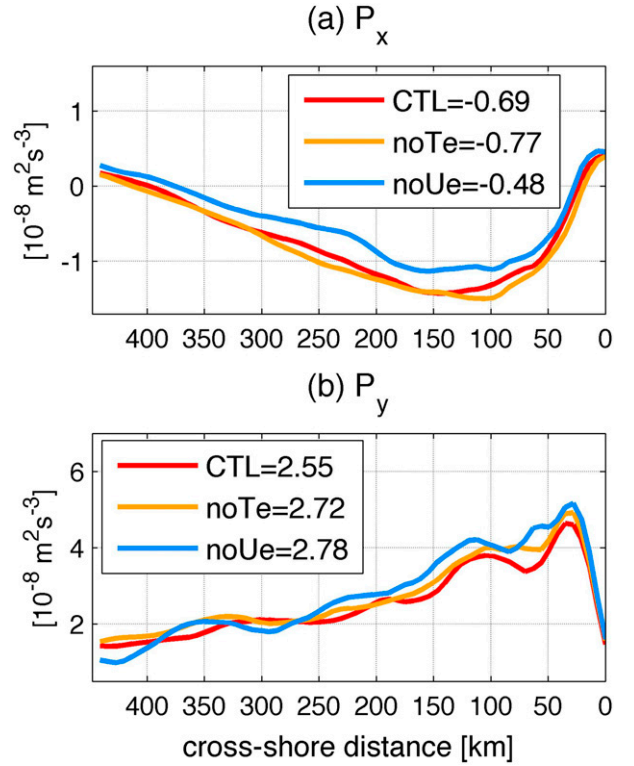

FIG. 9. As in Fig. 8, but showing the (a) zonal and (b) meridional components of the P term.

increase further the EKE. Despite the seemingly large difference in percentage changes, the changes in absolute magnitude are comparable between P_x and P_y; therefore, both terms should be of comparable importance in generating a lower EKE level in CTL.

5. Impact on Ekman pumping velocity

The change in wind stress via SST and surface current leads to anomalous Ekman pumping. This section examines the relative contribution from the SST and surface current on the Ekman pumping velocities in the CCS and how they are related to the eddy energetics in the CCS. When the Rossby number (Ro = ζ/f, the ratio of relative ζ to planetary f vorticity) is not small, the Ekman pumping depends on the total vorticity $f + \zeta$ (Stern 1965; Mahadevan et al. 2008), such that the total Ekman pumping velocity W_{TOT} can be approximated following Gaube et al. (2015) as

$$W_{\text{TOT}} = \frac{1}{\rho_0} \nabla \times \frac{\tau}{f + \zeta}$$
$$\approx \frac{\nabla \times \tau}{\rho_0(f + \zeta)} - \frac{\tau \times \nabla \zeta}{\rho_0(f + \zeta)^2} + \frac{\beta \tau_x}{\rho_0(f + \zeta)^2}. \quad (7)$$

The first term represents the curl of wind stress, which includes the effect of surface currents, and is termed the

consistent with the minimal change in wind stress and BC. On the other hand, there is a strong increase (~24%) in P in noU$_e$ over most of the cross-shelf distance; that is, suppressing the U_e effect on wind stress results in more wind energy transfer to the ocean, accounting for the large increase in EKE. Inspection of the zonal and meridional components of the eddy–wind interaction term provides further insights into the cause of this change (Fig. 9). Recall that the P_x is negative in the upwelling zone, damping the EKE. This damping effect in CTL is weakened in noU$_e$ by about 30%. The noT$_e$ case yields some (~11%) increase in the damping effect compared to CTL. The P_y shows that the positive wind energy input is increased when T_e is suppressed (by ~7%) and when U_e is suppressed (by ~10%), helping to

linear Ekman pumping. The second term arises from the wind stress acting on the vorticity gradient of the eddy, which is termed the nonlinear Ekman pumping. The third term, negligible, is associated with the interaction between β and τ_x. Since the SST effect on wind stress curl is included in the first term, Gaube et al. (2015) separated it from the background linear wind stress curl by spatially filtering out the SST-induced wind stress τ_e from the background wind stress τ_b. We use the 500-km lowess filter in this analysis to be consistent with the definition of small-scale features in the online smoothing. Therefore,

$$W_{\text{TOTe}} = \underbrace{\frac{\nabla \times \tau_b}{\rho_0(f + \zeta)}}_{W_{\text{LIN}}} + \underbrace{\frac{\nabla \times \tau_e}{\rho_0(f + \zeta)}}_{W_{\text{SST}}} - \underbrace{\frac{\tau_b \times \nabla\zeta}{\rho_0(f + \zeta)^2}}_{W_\zeta}. \quad (8)$$

The estimated total Ekman pumping velocity W_{TOTe} is the sum of the linear Ekman pumping W_{LIN} that takes into account the eddy-induced surface current but not the eddy SST, the eddy SST-driven Ekman pumping W_{SST} that is generated by the crosswind SST gradient, and the Ekman pumping that depends on gradient of surface vorticity W_ζ.

The W_{SST} is estimated by calculating the perturbation SST-driven wind stress curl $(\nabla \times \tau)'$ from the crosswind SST gradient $(\nabla T \times \hat{\tau})'$ using a quasi-linear relationship between the two $(\nabla \times \tau)' \approx S_c(\nabla T \times \hat{\tau})'$, where S_c is the linear regression coefficient (Chelton et al. 2007). Figure 10 compares the S_c from the satellite observations and the five SCOAR model outputs. It is important to note that S_c is obtained from the deviation from the monthly mean fields (Chelton et al. 2007) but is applied to the monthly averaged $(\nabla T \times \hat{\tau})$ to obtain the time-mean W_{SST} (P. Gaube 2014, personal communication). That way, the magnitude of the W_{SST} can be directly compared to the other terms estimated from the monthly mean fields.

The observations based on the NOAA OI SST and the QuikSCAT wind stress for the period of 2005–09 show a quasi-linear relationship between $(\nabla \times \tau)'$ and $(\nabla T \times \hat{\tau})'$ with coupling coefficients of $S_c = 0.78$ when calculated over the model domain. Note that this is lower than the estimate by Chelton et al. (2007) of $S_c = 2.13$ based on the AMSR-E SSTs for the upwelling zone (35°–45°N, 128°–118°W) in 2002–05. When the same domain is chosen for calculation, S_c increases to 1.03 but still smaller than their previous estimate. One difference is the much broader range of the crosswind SST gradient in our analysis [$\pm 2°$C $(100\,\text{km})^{-1}$] compared to Chelton et al.'s analysis [$\pm 1°$C $(100\,\text{km})^{-1}$]; this might be because the AMSR-E SSTs used in their analysis has a footprint size of 56 km and cannot detect the regime of large SST gradients within 100 km from the coast due to side-lobe contamination. This caveat is overcome to some extent by the use of the AVHRR-only SST dataset

merged with the nearshore in situ data on a high-resolution grid (¼°; Reynolds et al. 2007). Other reasons, such as a different period of temporal averaging, might account for the remaining differences.

The observed linearity is reasonably well reproduced in CTL, noU$_e$, and noU$_{\text{tot}}$, which contain the eddy SSTs and thus the associated crosswind SST gradients. Note that these runs contain a much wider range of the crosswind SST gradients, as much as $\pm 4°$C $(100\,\text{km})^{-1}$, but the linearity in wind stress curl response is well preserved even at the extreme ends of the distribution. In contrast, noT$_e$ and noT$_e$U$_e$ both feature very weak and insignificant linear regression coefficients with the limited range of the crosswind SST gradients. Using the resulting coupling coefficients, W_{SST} is estimated for each case and compared with two other terms: W_{LIN} and W_ζ.

Figure 11 shows the summertime mean Ekman pumping velocities (m day^{-1}) in 2005–09 from the observations and CTL. In both the observations and CTL, W_{LIN} is dominant in W_{TOTe} with magnitudes reaching more than 0.4 m day^{-1} upwelling near the coastal zone and comparatively weaker downwelling of 0.1–0.2 m day^{-1} in the broader offshore regions. The term W_{SST} is weakly positive in the upwelling zone near the coast, with typical values of 0.1–0.2 m day^{-1}, while it is negative in the lee of Pt. Conception and into the Southern California Bight. The term W_ζ shows noisy spatial structures reflecting the gradients of the vorticity of the eddy-induced surface currents. Large-scale patterns of W_{TOTe} are similar to W_{LIN}, but the detailed structure in W_{TOTe} is determined together by W_{SST} and W_ζ, suggesting that small-scale SSTs and surface currents are important in determining the climatological pattern of the Ekman pumping velocity. In noT$_e$ (Fig. 12, top), it is not surprising that W_{SST} vanishes; the small-scale structure of the W_{TOTe} climatology is determined by W_ζ. Likewise, in noU$_e$ (Fig. 12, bottom), W_ζ is negligible and W_{SST} becomes important for the small-scale structure of W_{TOTe}.

The terms W_{SST} and W_ζ have comparable magnitude and range of variability but very different spatial structures. Since W_{LIN} is independent of the eddy fields, it is nearly the same across the experiments. The difference in W_{TOTe} is, therefore, attributed to the difference in eddy fields, either via crosswind SST gradient or surface vorticity. Figure 13 shows the climatological difference in the W_{TOTe} between CTL and noT$_e$ (top) and that between CTL and noU$_e$ (bottom). The magnitudes of the differences exceed ± 0.3 m day^{-1} in both comparisons. The difference patterns visually correspond well to the differences in SST gradient ∇T in Fig. 13a (overlaid contours) and the surface vorticity ζ in Fig. 13c. The spatiotemporal correspondence is further quantified by constructing binned scatterplots between the difference in W_{TOTe} and the difference in ∇T (Fig. 13b) and
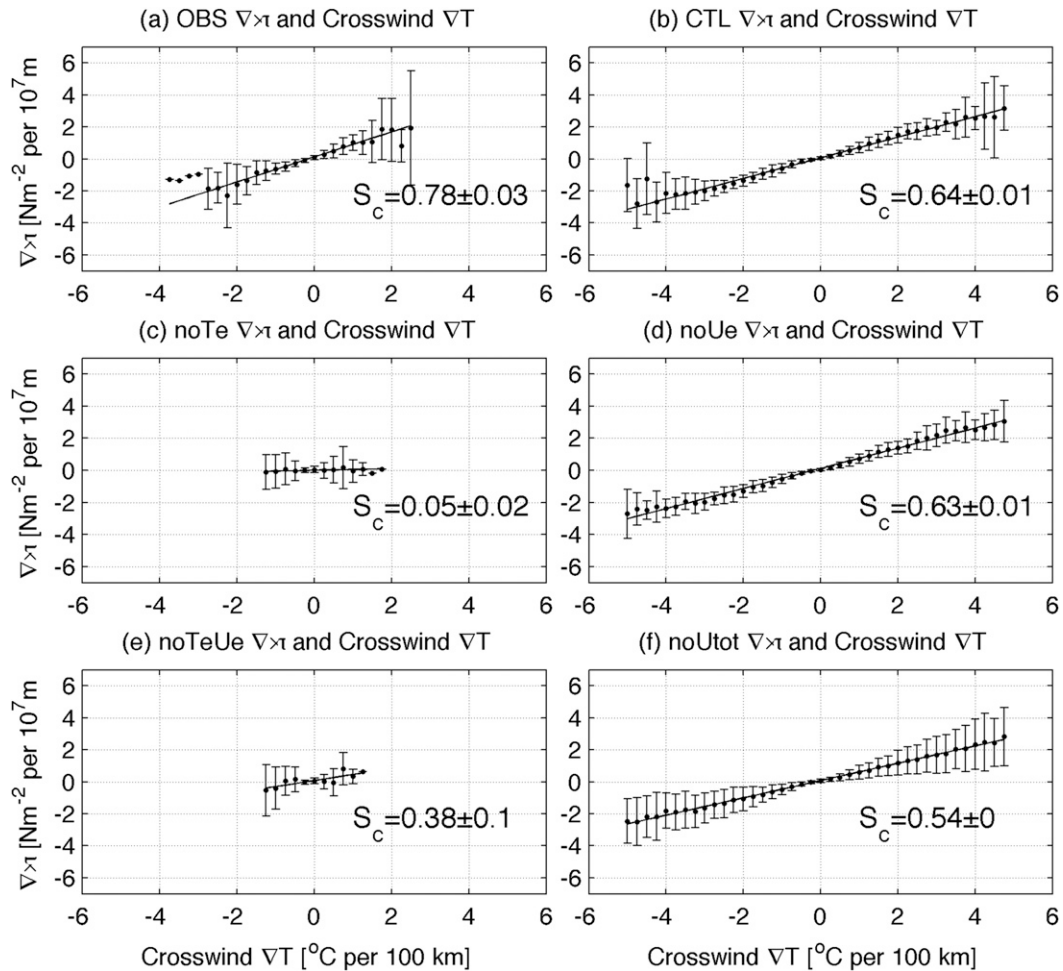
FIG. 10. Binned scatterplots between perturbation wind stress curls $(\nabla \times \tau)'$ [N m^{-2} $(10^4$ km$)^{-1}$] and perturbation crosswind SST gradient $\nabla T \times \hat{\tau}$ [°C $(100$ km$)^{-1}$] from (a) OBS, (b) CTL, (c) noT$_e$, (d) noU$_e$, (e) noT$_e$U$_e$, and (f) noU$_{tot}$ for July–September 2005–09 calculated over the entire model domain. The error bars represent the ± 1 standard deviation of the scatter within each bin. All slopes are statistically significant at $p = 0.01$ except for (c) and (e).

ζ (Fig. 13d). Both cases display strong linear relationships with a significant regression coefficient of $S_c = 0.05$ m day^{-1} [°C^{-1} $(100$ km$)^{-1}$]$^{-1}$ for the CTL-noT$_e$ case and $S_c = -0.25$ m day^{-1} day^{-1} for the CTL-noU$_e$.

The strong linear relationship in Fig. 13b confirms that the W$_{SST}$ preferentially affects the propagation of the eddy (Dewar and Flierl 1987). For a northerly wind over a cold-core cyclonic eddy, for example, the SST–wind relationship results in upwelling (downwelling) in the western (eastern) part of the eddy, helping it to propagate westward [see results from the idealized eddies or observed composite of the real eddies in Chelton (2013) and Gaube et al. (2015)]. The opposite is true for a warm-core anticyclonic eddy. In contrast, the strong negative relationship between ζ and the Ekman pumping in Fig. 13d suggests that the same cyclonic (anticyclonic) eddies induce anomalous downward (upward) Ekman pumping

velocities, acting to weaken the amplitudes of the eddies themselves regardless of the sense of rotation. These two effects are consistent with the result of the spatially averaged EKE difference showing that suppressing U_e produces the stronger eddy activity, while suppressing T_e has no significant effect.

6. Summary and discussion

The summertime California Current System (CCS) is characterized by persistent and energetic mesoscale eddies with typical anomalies in SST and cross-shore surface current exceeding 2°C and 0.5 m s^{-1}, respectively. For the first time, this study examines the relative effect of the small-scale eddy SST and surface current on the wind stress and Ekman pumping and the impact on the energetics and dynamic response of the
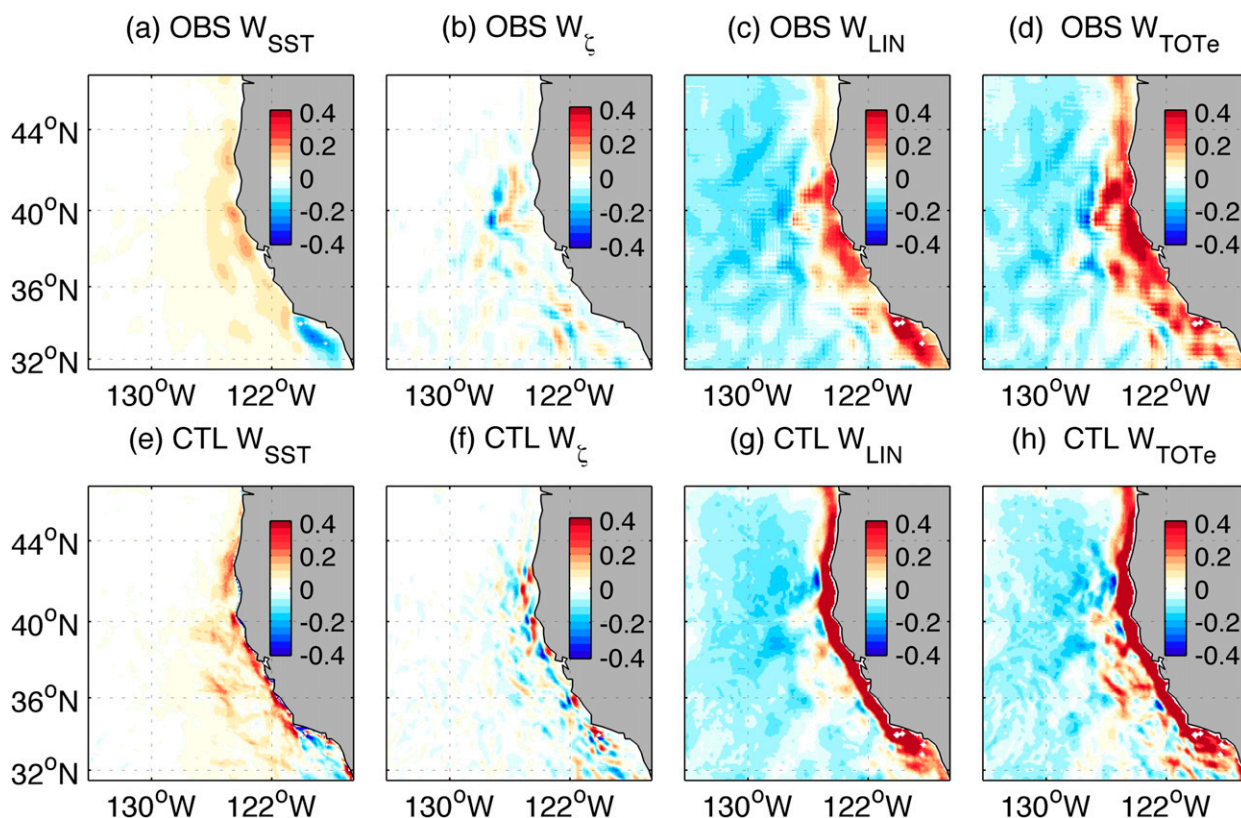
FIG. 11. July–September (2005–09) averaged (a),(e) SST-induced Ekman pumping (W_{SST}); (b),(f) vorticity gradient–induced Ekman pumping W_ζ; (c),(g) linear Ekman pumping W_{LIN}; and (d),(h) the estimated total Ekman pumping W_{TOTe}, which is the sum of the first three terms, from (top) observations and (bottom) CTL (units: m day^{-1}).

CCS. Our high-resolution (7 km) regional coupled model simulations capture the simultaneous coupling processes due to eddy-induced SST and currents, while the respective effects can be inferred from otherwise identical experiments with either coupling effect suppressed. The online smoothing procedure also allows distinguishing the eddy-driven coupling effect from that due to large-scale coupling.

In general, the results highlight the remarkably strong effect of eddy–wind interaction via surface current. The magnitude of the mean SST change is greater and extends farther offshore when the eddy current is allowed to affect the wind stress. The resulting change in SST is characterized by alternating elongated bands of positive and negative anomalies extending from the coast southwestward. This pattern is closely related to the change in onshore and offshore surface current anomalies. The simplified mixed layer heat budget suggests that the mean horizontal temperature advection between nearshore and offshore are mainly responsible for the emergence of the alternating SST anomaly patterns. The horizontal temperature advection by eddies offsets the mean advection, suggesting an active role of eddies

in determining the rectified time-mean SST response. The change in temperature advection by both the mean and eddy currents is greater with the effect of surface current on wind stress than that with SST. Therefore, the eddy current effect on wind stress causes the stronger dynamical response in the CCS.

The subsequent analysis of the EKE and the energy conversion process supports this conclusion. The EKE is considerably reduced when eddy–current interaction is included in the bulk parameterization, whereas eddy–SST interaction shows very little effect. The weakened EKE with the surface current effect is due to the increased surface eddy drag (Eden and Dietze 2009) and the reduced wind energy transfer (Hutchinson et al. 2010). Changes in baroclinic and barotropic conversion processes are comparatively small and hence unlikely to explain the difference in EKE.

Modified wind stress over the CCS eddies produces perturbation wind stress curl and Ekman pumping velocity through the crosswind SST gradient and the surface vorticity gradient. The resultant Ekman pumping velocities are of comparable magnitudes, but their juxtaposition with the SST gradient and the vorticity of the surface
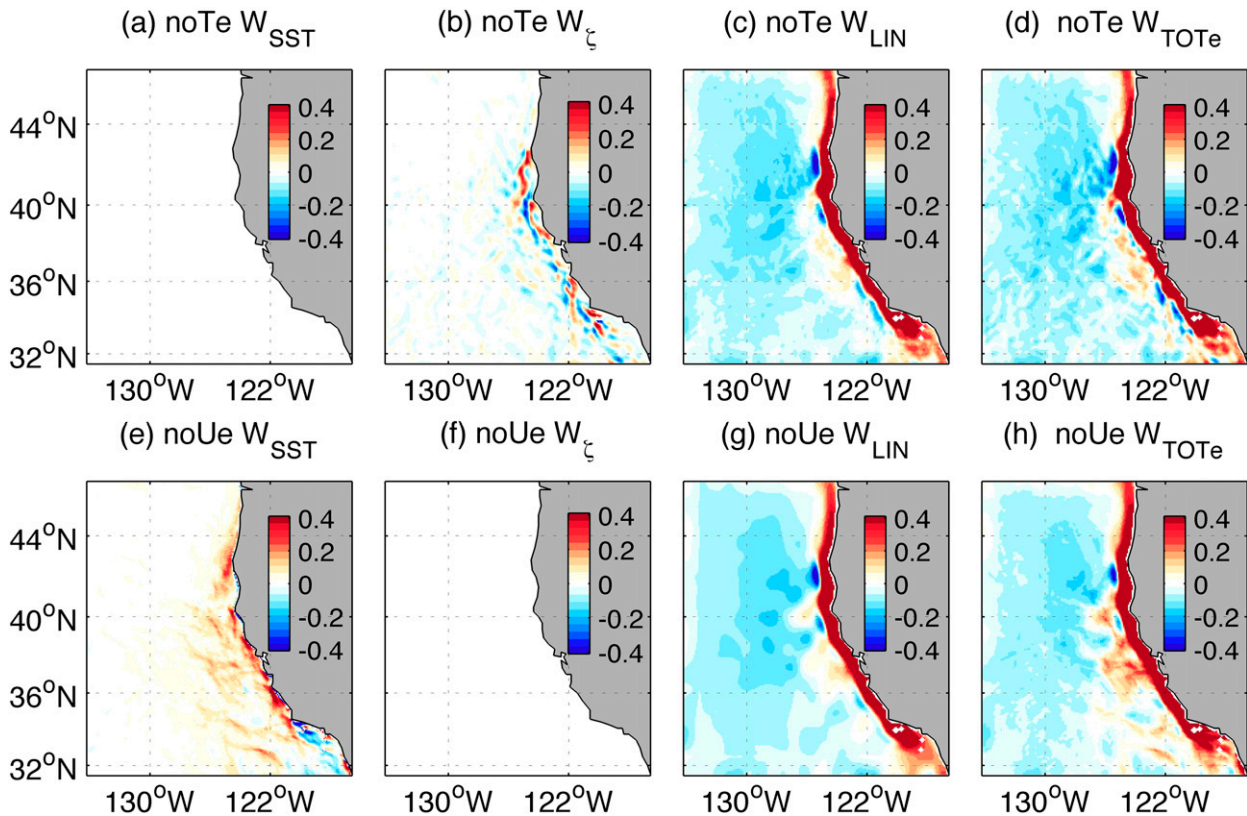
FIG. 12. As in Fig. 11, but for (top) noT$_e$ and (bottom) noU$_e$.

current implies different dynamical feedback mechanisms. The eddy current–induced Ekman downwelling (upwelling) are collocated with the cyclonic (anticyclonic) eddies, acting to attenuate the eddy amplitude. In contrast, the SST-induced Ekman upwelling (downwelling) is spatiotemporally well correlated with the positive (negative) SST gradients. Considering the 90° out-of-phase (quadrature) relationship between the SST/SSH and their gradients in typical cold-core cyclonic and warm-core anticyclonic eddies (e.g., Gaube et al. 2014, 2015), this SST-induced Ekman pumping velocity would preferentially influence the propagation of the eddies. The implied feedback effects of the current- and SST-induced Ekman pumping velocity on the eddy activity are consistent with the interpretation of the spatially averaged EKE response. Further eddy-centric analysis is needed to examine the changes in propagation characteristics of the eddies using a Lagrangian eddy-tracking procedure (Jin et al. 2009; Kurian et al. 2011; Gaube et al. 2014; 2015); this also is a topic of a future study.

The results imply that, for the ocean-only model forced with wind products that do not include the ocean current effect (e.g., atmospheric reanalyses), the inclusion of the surface current in the bulk formula for wind stress would help to improve the model simulations in terms of

energetics of the ocean circulation and mesoscale eddies (Fig. 4; see also Xu and Scott 2008). However, the same statement may not be true for ocean models forced with scatterometer estimates of the 10-m wind field since the wind estimates are already based on the moving ocean surface. The mismatch between the prescribed (observed) current effects contained in the QuikSCAT and the simulated currents (occurring with random phase) would lead to misrepresentation of the two small-scale processes that require the covariance between the surface current and wind stress, that is, the surface drag and the wind work, as demonstrated in this study. This small-scale error would lead to a possible source of large-scale bias through their effects on surface stress and Ekman pumping. For this reason, the use of "absolute" winds is advised to force the global ocean–sea ice model, which is in agreement with the recommendation from WCRP (2015).

Overall, this study demonstrates the remarkably strong effect of the eddy surface current on the Ekman pumping, the eddy energetics, and the dynamics of the current system in the CCS. Given the persistent and nontrivial amplitude of the rectified response in SST climatology (>±1°C), some ensuing important atmospheric feedback effect is expected by the current–wind coupling in the CCS, for example, on the low-level stratiform cloudiness
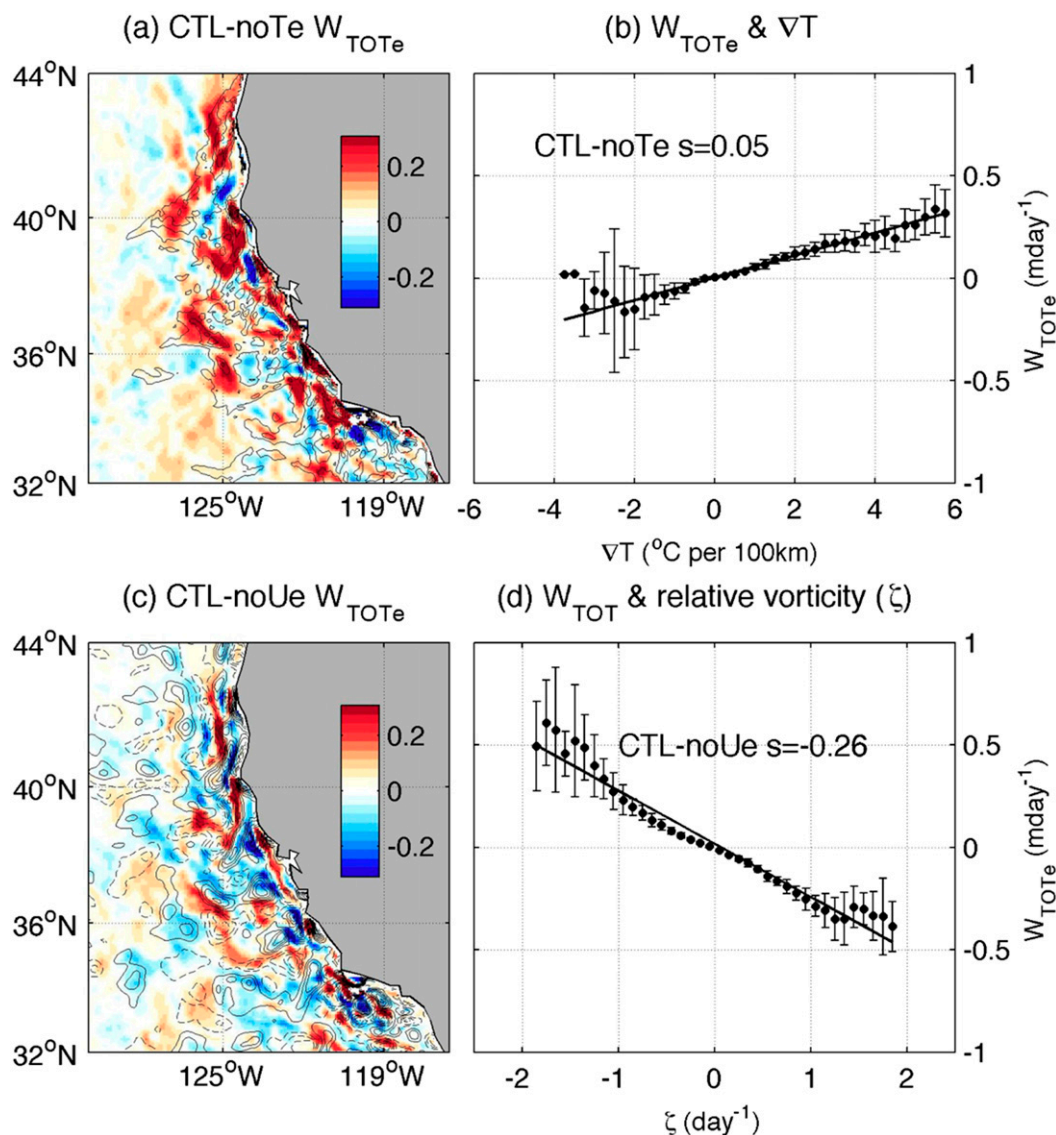
FIG. 13. (left) July–September (2005–09) mean difference in the estimated total Ekman pumping velocity W_{TOTe} (shading; m day^{-1}) overlaid with (a) difference in SST gradient [°C (100 km)$^{-1}$, CI = 1, zero contours suppressed] and (c) surface vorticity (s^{-1}, CI = 0.2, zero contours suppressed). (right) Binned scatterplots between the difference in W_{TOTe} and the difference in (b) SST gradient and (d) surface vorticity. All slopes are statistically significant at $p = 0.01$.

and the surface radiation budget (e.g., Klein and Hartmann 1993; Norris and Leovy 1994; Schwartz et al. 2014). The effect is likely to be also important in other oceanic regions with strong eddy activities or semipermanent frontal zones such as western boundary currents. In those regions, the eddy current coupling effect exerts continuous influence on wind stress both in summer and winter, while the SST–wind coupling effect might cease to be important in summer without strong SST gradients. The resultant rectified response of low-level baroclinicity and storm track variability in the atmosphere has not been demonstrated or quantified in the literature. To the extent that the eddy current effect is important in the SST, the so-called frontal-scale air–sea interactions, primarily treated as the SST-driven air–sea coupling process, will need to consider the effect of eddy dynamics and oceanic currents as an alternative coupled ocean–atmosphere mechanism that could play an important role in the climate system.

REFERENCES

Anderson, L., D. McGillicuddy, M. Maltrud, I. Lima, and S. Doney, 2011: Impact of eddy–wind interaction on eddy demographics and phytoplankton community structure in a model of the North Atlantic Ocean. *Dyn. Atmos. Oceans*, **52**, 80–94, doi:10.1016/j.dynatmoce.2011.01.003.

Beljaars, A. C. M., 1995: The parameterization of surface fluxes in large-scale models under free convection. *Quart. J. Roy. Meteor. Soc.*, **121**, 255–270, doi:10.1002/qj.49712152203.

Boé, J., A. Hall, F. Colas, J. C. McWilliams, X. Qu, J. Kurian, S. B. Kapnick, and H. Frenzel, 2011: What shapes mesoscale wind anomalies in coastal upwelling zones? *Climate Dyn.*, **36**, 2037–2049, doi:10.1007/s00382-011-1058-5.

Brink, K., 2016: Continental shelf baroclinic instability. Part I: Relaxation from upwelling or downwelling. *J. Phys. Oceanogr.*, doi:10.1175/JPO-D-15-0047.1, in press.

——, and H. Seo, 2016: Continental shelf baroclinic instability. Part II: Oscillating wind forcing. *J. Phys. Oceanogr.*, doi:10.1175/JPO-D-15-0048.1, in press.

Bye, J. A. T., 1986: Momentum exchange at the sea surface by wind stress and understress. *Quart. J. Roy. Meteor. Soc.*, **112**, 501–510, doi:10.1002/qj.49711247212.

Caniaux, G., and S. Planton, 1998: A three-dimensional ocean mesoscale simulation using data from the SEMAPHORE experiment: Mixed layer heat budget. *J. Geophys. Res.*, **103**, 25 081–25 099, doi:10.1029/98JC00452.

Capet, X. J., P. Marchesiello, and J. C. McWilliams, 2004: Upwelling response to coastal wind profiles. *Geophys. Res. Lett.*, **31**, L13311, doi:10.1029/2004GL020123.

Carton, J. A., and B. S. Giese, 2008: A reanalysis of ocean climate using Simple Ocean Data Assimilation (SODA). *Mon. Wea. Rev.*, **136**, 2999–3017, doi:10.1175/2007MWR1978.1.

Castelao, R. M., T. P. Mavor, J. A. Barth, and L. C. Breaker, 2006: Sea surface temperature fronts in the California Current System from geostationary satellite observations. *J. Geophys. Res.*, **111**, C09026, doi:10.1029/2006JC003541.

Centurioni, L., J. Ohlmann, and P. Niiler, 2008: Permanent meanders in the California Current System. *J. Phys. Oceanogr.*, **38**, 1690–1710, doi:10.1175/2008JPO3746.1.

Chelton, D. B., 2013: Ocean–atmosphere coupling: Mesoscale eddy effects. *Nat. Geosci.*, **6**, 594–595, doi:10.1038/ngeo1906.

——, and M. G. Schlax, 1994: The resolution capability of an irregularly sampled dataset: With application to Geosat altimeter data. *J. Atmos. Oceanic Technol.*, **11**, 534–550, doi:10.1175/1520-0426(1994)011<0534:TRCOAI>2.0.CO;2.

——, and S.-P. Xie, 2010: Coupled ocean–atmosphere interaction at oceanic mesoscales. *Oceanography*, **23**, 52–69, doi:10.5670/oceanog.2010.05.

——, and Coauthors, 2001: Observations of coupling between surface wind stress and sea surface temperature in the eastern tropical Pacific. *J. Climate*, **14**, 1479–1498, doi:10.1175/1520-0442(2001)014<1479:OOCBSW>2.0.CO;2.

——, M. G. Schlax, M. H. Freilich, and R. F. Milliff, 2004: Satellite measurements reveal persistent small-scale features in ocean winds. *Science*, **303**, 978–983, doi:10.1126/science.1091901.

——, ——, and R. M. Samelson, 2007: Summertime coupling between sea surface temperature and wind stress in the California Current System. *J. Phys. Oceanogr.*, **37**, 495–517, doi:10.1175/JPO3025.1.

Chen, F., and J. Dudhia, 2001: Coupling an advanced land-surface/hydrology model with the Penn State/NCAR MM5 modeling system. Part I: Model implementation and sensitivity. *Mon. Wea. Rev.*, **129**, 569–585, doi:10.1175/1520-0493(2001)129<0569:CAALSH>2.0.CO;2.

Chou, M.-D., and M. J. Suarez, 1999: A solar radiation parameterization for atmospheric studies. NASA Tech. Rep. NASA/TM-1999-10460, 38 pp. [Available online at http://gmao.gsfc.nasa.gov/pubs/docs/Chou136.pdf.]

Cleveland, W., 1979: Robust locally weighted regression and smoothing scatterplots. *J. Amer. Stat. Assoc.*, **74**, 829–836, doi:10.1080/01621459.1979.10481038.

——, and S. J. Devlin, 1988: Locally weighted regression: An approach to regression analysis by local fitting. *J. Amer. Stat. Assoc.*, **83**, 596–610.

Cornillon, P., and K.-A. Park, 2001: Warm core ring velocities inferred from NSCAT. *Geophys. Res. Lett.*, **28**, 575–578, doi:10.1029/2000GL011487.

da Silva, A. M., C. Young-Molling, and S. Levitus, 1994: *Algorithms and Procedures*. Vol. 1, *Atlas of Surface Marine Data 1994*, NOAA Atlas NESDIS 6, 83 pp.

Dewar, W., and G. Flierl, 1987: Some effects of the wind on rings. *J. Phys. Oceanogr.*, **17**, 1653–1667, doi:10.1175/1520-0485(1987)017<1653:SEOTWO>2.0.CO;2.

Dorman, C. E., and D. Koračin, 2008: Interaction of the summer marine layer with an extreme California coastal bend. *Mon. Wea. Rev.*, **136**, 2894–2922, doi:10.1175/2007MWR2336.1.

Duhaut, T. H. A., and D. N. Straub, 2006: Wind stress dependence on ocean surface velocity: Implications for mechanical energy input to ocean circulation. *J. Phys. Oceanogr.*, **36**, 202–211, doi:10.1175/JPO2842.1.

Eden, C., and H. Dietze, 2009: Effects of mesoscale eddy/wind interactions on biological new production and eddy kinetic energy. *J. Geophys. Res.*, **114**, C05023, doi:10.1029/2008JC005129.

Fairall, C., E. F. Bradley, J. Godfrey, G. Wick, J. Edson, and G. Young, 1996: Cool-skin and warm-layer effects on sea surface temperature. *J. Geophys. Res.*, **101**, 1295–1308, doi:10.1029/95JC03190.

——, ——, J. Hare, A. Grachev, and J. Edson, 2003: Bulk parameterization of air–sea fluxes: Updates and verification for the COARE algorithm. *J. Climate*, **16**, 571–591, doi:10.1175/1520-0442(2003)016<0571:BPOASF>2.0.CO;2.

Frenger, I., N. Gruber, R. Knutti, and M. Münnich, 2013: Imprint of Southern Ocean eddies on winds, clouds and rainfall. *Nat. Geosci.*, **6**, 608–612, doi:10.1038/ngeo1863.

Gaube, P., D. J. McGillicuddy Jr., D. B. Chelton, M. J. Behrenfeld, and P. G. Strutton, 2014: Regional variations in the influence of mesoscale eddies on near-surface chlorophyll. *J. Geophys. Res. Oceans*, **119**, 8195–8220, doi:10.1002/2014JC010111.

——, D. B. Chelton, R. M. Samelson, M. G. Schlax, and L. W. O'Neill, 2015: Satellite observations of mesoscale eddy-induced Ekman pumping. *J. Phys. Oceanogr.*, **45**, 104–132, doi:10.1175/JPO-D-14-0032.1.

Giese, B. S., and S. Ray, 2011: El Niño variability in Simple Ocean Data Assimilation (SODA), 1871–2008. *J. Geophys. Res.*, **116**, C02024, doi:10.1029/2010JC006695.

Haack, T., D. Chelton, J. Pullen, J. D. Doyle, and M. Schlax, 2008: Summertime influence of SST on surface wind stress off the U.S. West Coast from the U.S. Navy COAMPS model. *J. Phys. Oceanogr.*, **38**, 2414–2437, doi:10.1175/2008JPO3870.1.

Haidvogel, D. B., H. G. Arango, K. Hedstrom, A. Beckmann, P. Malanotte-Rizzoli, and A. F. Shchepetkin, 2000: Model evaluation experiments in the North Atlantic basin: Simulations in nonlinear terrain-following coordinates. *Dyn. Atmos. Oceans*, **32**, 239–281, doi:10.1016/S0377-0265(00)00049-X.

Hayes, S. P., M. J. McPhadden, and J. M. Wallace, 1989: The influence of sea surface temperature on surface wind in the eastern equatorial Pacific: Weekly to monthly variability. *J. Climate*, **2**, 1500–1506, doi:10.1175/1520-0442(1989)002<1500:TIOSST>2.0.CO;2.

Hong, S.-Y., J. Dudhia, and S.-H. Chen, 2004: A revised approach to ice microphysical processes for the bulk parameterization of clouds and precipitation. *Mon. Wea. Rev.*, **132**, 103–120, doi:10.1175/1520-0493(2004)132<0103:ARATIM>2.0.CO;2.

——, Y. Noh, and J. Dudhia, 2006: A new vertical diffusion package with an explicit treatment of entrainment processes. *Mon. Wea. Rev.*, **134**, 2318–2341, doi:10.1175/MWR3199.1.

Hughes, C. W., and C. Wilson, 2008: Wind work on the geostrophic ocean circulation: An observational study of the effect of small scales in the wind stress. *J. Geophys. Res.*, **113**, C02016, doi:10.1029/2007JC004371.

Hutchinson, D. K., A. M. C. Hogg, and J. R. Blundell, 2010: Southern Ocean response to relative velocity wind stress forcing. *J. Phys. Oceanogr.*, **40**, 326–339, doi:10.1175/2009JPO4240.1.

Jin, X., C. Dong, J. Kurian, J. C. McWilliams, D. B. Chelton, and Z. Li, 2009: SST–wind interaction in coastal upwelling: Oceanic simulation with empirical coupling. *J. Phys. Oceanogr.*, **39**, 2957–2970, doi:10.1175/2009JPO4205.1.

Juang, H.-M. H., and M. Kanamitsu, 1994: The NMC nested regional spectral model. *Mon. Wea. Rev.*, **122**, 3–26, doi:10.1175/1520-0493(1994)122<0003:TNNRSM>2.0.CO;2.

Kain, J. S., 2004: The Kain–Fritsch convective parameterization: An update. *J. Appl. Meteor.*, **43**, 170–181, doi:10.1175/1520-0450(2004)043<0170:TKCPAU>2.0.CO;2.

Kelly, K. A., S. Dickinson, M. J. McPhaden, and G. C. Johnson, 2001: Ocean currents evident in satellite wind data. *Geophys. Res. Lett.*, **28**, 2469–2472, doi:10.1029/2000GL012610.

Klein, S. A., and D. L. Hartmann, 1993: The seasonal cycle of low stratiform clouds. *J. Climate*, **6**, 1587–1606, doi:10.1175/1520-0442(1993)006<1587:TSCOLS>2.0.CO;2.

Koračin, D., C. E. Dorman, and E. P. Dever, 2004: Coastal perturbations of marine-layer winds, wind stress, and wind stress curl along California and Baja California in June 1999. *J. Phys. Oceanogr.*, **34**, 1152–1173, doi:10.1175/1520-0485(2004)034<1152:CPOMWW>2.0.CO;2.

Kurian, J., F. Colas, X. Capet, J. C. McWilliams, and D. B. Chelton, 2011: Eddy properties in the California Current System. *J. Geophys. Res.*, **116**, C08027, doi:10.1029/2010JC006895.

Large, W. G., J. C. McWilliams, and S. C. Doney, 1994: Oceanic vertical mixing: A review and a model with a nonlocal boundary layer parameterization. *Rev. Geophys.*, **32**, 363–403, doi:10.1029/94RG01872.

Ledwell, J., D. McGillicuddy Jr., and L. Anderson, 2008: Nutrient flux into an intense deep chlorophyll layer in a mode-water eddy. *Deep-Sea Res. II*, **55**, 1139–1160, doi:10.1016/j.dsr2.2008.02.005.

Luo, J.-J., S. Masson, E. Roeckner, G. Madec, and T. Yamagata, 2005: Reducing climatology bias in an ocean–atmosphere CGCM with improved coupling physics. *J. Climate*, **18**, 2344–2360, doi:10.1175/JCLI3404.1.

Mahadevan, A., L. Thomas, and A. Tandon, 2008: Comment on "Eddy/wind interactions stimulate extraordinary mid-ocean plankton blooms." *Science*, **320**, 448, doi:10.1126/science.1152111.

Maloney, E. D., and D. B. Chelton, 2006: An assessment of the sea surface temperature influence on surface wind stress in numerical weather prediction and climate models. *J. Climate*, **19**, 2743–2762, doi:10.1175/JCLI3728.1.

Marchesiello, P., J. C. McWilliams, and A. Shchepetkin, 2003: Equilibrium structure and dynamics of the California Current System. *J. Phys. Oceanogr.*, **33**, 753–783, doi:10.1175/1520-0485(2003)33<753:ESADOT>2.0.CO;2.

Martin, A., and K. Richards, 2001: Mechanisms for vertical nutrient transport within a North Atlantic mesoscale eddy. *Deep-Sea Res. II*, **48**, 757–773, doi:10.1016/S0967-0645(00)00096-5.

Masina, S., S. Philander, and A. Bush, 1999: An analysis of tropical instability waves in a numerical model of the Pacific Ocean: 2. Generation and energetics of the waves. *J. Geophys. Res.*, **104**, 29 637–29 662, doi:10.1029/1999JC900226.

McGillicuddy, D. J., 2015: Formation of intrathermocline lenses by eddy–wind interaction. *J. Phys. Oceanogr.*, **45**, 606–612, doi:10.1175/JPO-D-14-0221.1.

——, and Coauthors, 2007: Eddy/wind interactions stimulate extraordinary mid-ocean plankton blooms. *Science*, **316**, 1021–1026, doi:10.1126/science.1136256.

Mlawer, E. J., S. J. Taubman, P. D. Brown, M. J. Iacono, and S. A. Clough, 1997: Radiative transfer for inhomogeneous atmospheres: RRTM, a validated correlated-k model for the longwave. *J. Geophys. Res.*, **102**, 16 663–16 682, doi:10.1029/97JD00237.

Moisan, J. R., and P. P. Niiler, 1998: The seasonal heat budget of the North Pacific: Net heat flux and heat storage rates (1950–1990). *J. Phys. Oceanogr.*, **28**, 401–421, doi:10.1175/1520-0485(1998)028<0401:TSHBOT>2.0.CO;2.

Norris, J. R., and C. B. Leovy, 1994: Interannual variability in stratiform cloudiness and sea surface temperature. *J. Climate*, **7**, 1915–1925, doi:10.1175/1520-0442(1994)007<1915:IVISCA>2.0.CO;2.

O'Neill, L. W., S. K. Esbensen, N. Thum, R. M. Samelson, and D. B. Chelton, 2010: Dynamical analysis of the boundary layer and surface wind responses to mesoscale SST perturbations. *J. Climate*, **23**, 559–581, doi:10.1175/2009JCLI2662.1.

——, D. B. Chelton, and S. K. Esbensen, 2012: Covariability of surface wind and stress responses to sea surface temperature fronts. *J. Climate*, **25**, 5916–5942, doi:10.1175/JCLI-D-11-00230.1.

Pacanowski, R. C., 1987: Effect of equatorial currents on surface stress. *J. Phys. Oceanogr.*, **17**, 833–838, doi:10.1175/1520-0485(1987)017<0833:EOECOS>2.0.CO;2.

Park, K.-A., and P. C. Cornillon, 2002: Stability-induced modification of sea surface winds over Gulf Stream rings. *Geophys. Res. Lett.*, **29**, 2211, doi:10.1029/2001GL014236.

Paulson, C. A., and J. J. Simpson, 1977: Irradiance measurements in the upper ocean. *J. Phys. Oceanogr.*, **7**, 952–956, doi:10.1175/1520-0485(1977)007<0952:IMITUO>2.0.CO;2.

Putrasahan, D. A. J. M., A. J. Miller, and H. Seo, 2013a: Isolating mesoscale coupled ocean–atmosphere interactions in the Kuroshio Extension region. *Dyn. Atmos. Oceans*, **63**, 60–78, doi:10.1016/j.dynatmoce.2013.04.001.

——, ——, and ——, 2013b: Regional coupled ocean–atmosphere downscaling in the Southeast Pacific: Impacts on upwelling, mesoscale air–sea fluxes, and ocean eddies. *Ocean Dyn.*, **63**, 463–488, doi:10.1007/s10236-013-0608-2.

Renault, L., A. Hall, and J. C. McWilliams, 2016: Orographic shaping of US west coast wind profiles during the upwelling season. *Climate Dyn.*, **46**, 273–289, doi:10.1007/s00382-015-2583-4.

Reynolds, R. W., T. M. Smith, C. Liu, D. B. Chelton, K. S. Casey, and M. G. Schlax, 2007: Daily high-resolution-blended analyses for sea surface temperature. *J. Climate*, **20**, 5473–5496, doi:10.1175/2007JCLI1824.1.

Samelson, R., E. Skyllingstad, D. Chelton, S. Esbensen, L. O'Neill, and N. Thum, 2006: On the coupling of wind stress and sea surface temperature. *J. Climate*, **19**, 1557–1566, doi:10.1175/JCLI3682.1.

Schlax, M., D. B. Chelton, and M. H. Freilich, 2001: Sampling errors in wind fields constructed from single and tandem scatterometer datasets. *J. Atmos. Oceanic Technol.*, **18**, 1014–1036, doi:10.1175/1520-0426(2001)018<1014:SEIWFC>2.0.CO;2.

Schwartz, R. E., A. Gershunov, S. F. Iacobellis, and D. R. Cayan, 2014: North American west coast summer low cloudiness: Broadscale variability associated with sea surface temperature. *Geophys. Res. Lett.*, **41**, 3307–3314, doi:10.1002/2014GL059825.

Seo, H., and S.-P. Xie, 2011: Response and impact of equatorial ocean dynamics and tropical instability waves in the tropical Atlantic under global warming: A regional coupled downscaling study. *J. Geophys. Res. Oceans*, **116**, C03026, doi:10.1029/2010JC006670.

——, and ——, 2013: Impact of ocean warm layer thickness on the intensity of Hurricane Katrina in a regional coupled model. *Meteor. Atmos. Phys.*, **122**, 19–32, doi:10.1007/s00703-013-0275-3.

——, M. Jochum, R. Murtugudde, and A. J. Miller, 2006: Effect of ocean mesoscale variability on the mean state of tropical Atlantic climate. *Geophys. Res. Lett.*, **33**, L09606, doi:10.1029/2005GL025651.

——, ——, ——, ——, and J. O. Roads, 2007a: Feedback of tropical instability wave-induced atmospheric variability onto the ocean. *J. Climate*, **20**, 5842–5855, doi:10.1175/JCLI4330.1.

——, A. J. Miller, and J. O. Roads, 2007b: The Scripps Coupled Ocean–Atmosphere Regional (SCOAR) model, with applications in the eastern Pacific sector. *J. Climate*, **20**, 381–402, doi:10.1175/JCLI4016.1.

——, M. Jochum, R. Murtugudde, A. J. Miller, and J. O. Roads, 2008a: Precipitation from African easterly waves in a coupled model of the tropical Atlantic. *J. Climate*, **21**, 1417–1431, doi:10.1175/2007JCLI1906.1.

——, R. Murtugudde, M. Jochum, and A. J. Miller, 2008b: Modeling of mesoscale coupled ocean–atmosphere interaction and its feedback to ocean in the western Arabian Sea. *Ocean Modell.*, **25**, 120–131, doi:10.1016/j.ocemod.2008.07.003.

——, S.-P. Xie, R. Murtugudde, M. Jochum, and A. J. Miller, 2009: Seasonal effects of Indian Ocean freshwater forcing in a regional coupled model. *J. Climate*, **22**, 6577–6596, doi:10.1175/2009JCLI2990.1.

——, A. C. Subramanian, A. J. Miller, and N. R. Cavanaugh, 2014: Coupled impacts of the diurnal cycle of sea surface temperature on the Madden–Julian oscillation. *J. Climate*, **27**, 8422–8443, doi:10.1175/JCLI-D-14-00141.1.

Shchepetkin, A. F., and J. C. McWilliams, 2005: The Regional Oceanic Modeling System (ROMS): A split-explicit, free-surface, topography-following-coordinate ocean model. *Ocean Modell.*, **9**, 347–404, doi:10.1016/j.ocemod.2004.08.002.

Skamarock, W. C., and Coauthors, 2008: A description of the Advanced Research WRF version 3. NCAR Tech. Note NCAR/TN-475+STR, 113 pp. [Available online at http://www.mmm.ucar.edu/wrf/users/docs/arw_v3_bw.pdf.]

Small, R. J., and Coauthors, 2008: Air–sea interaction over ocean fronts and eddies. *Dyn. Atmos. Oceans*, **45**, 274–319, doi:10.1016/j.dynatmoce.2008.01.001.

——, K. J. Richards, S.-P. Xie, P. Dutrieux, and T. Miyama, 2009: Damping of tropical instability waves caused by the action of surface currents on stress. *J. Geophys. Res.*, **114**, C04009, doi:10.1029/2008JC005147.

Song, Q., D. B. Chelton, S. K. Esbensen, N. Thum, and L. W. O. Neil, 2009: Coupling between sea surface temperature and low-level winds in mesoscale numerical models. *J. Climate*, **22**, 146–164, doi:10.1175/2008JCLI2488.1.

Stern, M., 1965: Interaction of a uniform wind stress with a geostrophic vortex. *Deep-Sea Res. Oceanogr. Abstr.*, **12**, 355–367, doi:10.1016/0011-7471(65)90007-0.

Stevenson, J. W., and P. P. Niiler, 1983: Upper ocean heat budget during the Hawaii-to-Tahiti shuttle experiment. *J. Phys. Oceanogr.*, **13**, 1894–1907, doi:10.1175/1520-0485(1983)013<1894:UOHBDT>2.0.CO;2.

Strub, P. T., and C. James, 2000: Altimeter-derived variability of surface velocities in the California Current System: 2. Seasonal circulation and eddy statistics. *Deep-Sea Res. II*, **47**, 831–870, doi:10.1016/S0967-0645(99)00129-0.

Wallace, J. M., T. P. Mitchell, and C. Deser, 1989: The influence of sea surface temperature on surface wind in the eastern equatorial Pacific: Seasonal and interannual variability. *J. Climate*, **2**, 1492–1499, doi:10.1175/1520-0442(1989)002<1492:TIOSST>2.0.CO;2.

WCRP, 2015: CLIVAR Ocean Model Development Panel (OMDP) mini workshop on forcing ocean and sea-ice models. WCRP Rep. 9, CLIVAR Rep. 202, 21 pp. [Available online at http://www.clivar.org/sites/default/files/documents/OMDP_Grenoble_report.pdf.]

Xie, S.-P., 2004: Satellite observations of cool ocean–atmosphere interaction. *Bull. Amer. Meteor. Soc.*, **85**, 195–209, doi:10.1175/BAMS-85-2-195.

Xu, Y., and R. B. Scott, 2008: Subtleties in forcing eddy resolving ocean models with satellite wind data. *Ocean Modell.*, **20**, 240–251, doi:10.1016/j.ocemod.2007.09.003.

Yu, L., and R. A. Weller, 2007: Objectively analyzed air–sea heat fluxes for the global ice-free oceans (1981–2005). *Bull. Amer. Meteor. Soc.*, **88**, 527–539, doi:10.1175/BAMS-88-4-527.

Zhai, X., and R. J. Greatbatch, 2007: Wind work in a model of the northwest Atlantic Ocean. *Geophys. Res. Lett.*, **34**, L04606, doi:10.1029/2006GL028907.